Journal of Hydrology 669 (2026) 135081

Contents lists available at ScienceDirect

Journal of Hydrology

journal homepage: www.elsevier.com/locate/jhydrol

Understanding the limits of two lumped hydrological models through divergences between daily and sub-daily projections

Virginie Destuynder*, Siavash Pouryousefi Markhali, Annie Poulin

École de technologie supérieure (ÉTS), 1100 Rue Notre Dame O., Montréal, H3C 1K3, Québec, Canada

HIGHLIGHTS

- Time-step dependent hydrological projections include short and long-term divergences.
- Compensatory mechanisms cause inconsistent simulations under non-stationary conditions.
- The choice of time-step influences the projections of both hydrographs and floods.
- Time-step dependent projections can reveal shifts in runoff generation mechanisms.
- Realistic subsurface storage calibration improves hydrological projections' reliability.

ARTICLE INFO

This manuscript was handled by Marco Borga, Editor-in-Chief, with the assistance of Kolbjorn Engeland, Associate Editor

Keywords:
Hydrological modeling
Temporal resolution
Climate change
Flood projections

ABSTRACT

The present paper identifies four common reasons for divergences between projections of flow metrics simulated by lumped conceptual hydrological models at a daily time step, and a daily-averaged 3-h time step. These reasons are based on five case studies simulated by two hydrological models in North America in the context of climate change, and are related to: the filtering of subdaily discrete and cyclic processes; the time-step dependent solving of nonlinear equations involving logical conditions; the time-step dependent solving of nonlinear sequential equations; and the timing of the flood events within the daily window. The time-step dependent simulation of the corresponding internal processes requires compensatory mechanisms in other processes in order to achieve an equivalent performance of the hydrological models in calibration at both time steps. These compensatory mechanisms can be identified in the parameter sets of the models and often imply a time-step dependent seasonality of the internal variables. Divergences between hydrological projections at daily and subdaily time steps reveal significant future shifts in the hydrological regime or in the runoff-generating processes, outside the domain of validity of the calibrated parameter sets. Time-step dependent projections underscore the need for detailed insight before using projections for engineering applications. Furthermore, the comparison of hydrological simulations from different time steps is a valuable approach to assess the domain of validity of calibrated parameter sets, and to understand the behavior of conceptual hydrological models under non-stationary climate conditions.

1. Introduction

Since the 1990s, automatic hydrometric stations have been installed across North America, providing streamflow time series long enough for subdaily hydrological modeling studies (Comisión Nacional del Agua, 2016; Ministère de l'Environnement, de la Lutte contre les changements climatiques, de la Faune et des Parcs, 2020; U.S. Geological Survey, 2021). However, the network of hourly meteorological stations, which also provides input data for hydrological modeling, is not always adequate to correctly calibrate and validate the hydrological models across a large sample of watersheds, since its density, quality and configuration are highly heterogeneous. Earlier studies relying on high-resolution climate grids have nonetheless successfully calibrated lumped and distributed hydrological models (Bastola and Misra, 2013; Markhali et al., 2022a).

1.1. Impact of the temporal resolution on performance of hydrological models

Given the availability of fine-resolution hydroclimatic data, some studies have examined the impact of temporal resolution on the

* Corresponding author.
Email addresses: cc-virginie.destuynder@etsmtl.ca (V. Destuynder), siavash.pouryousefi-markhali@etsmtl.ca (S.P. Markhali), annie.poulin@etsmtl.ca (A. Poulin).

https://doi.org/10.1016/j.jhydrol.2026.135081
Received 6 June 2025; Received in revised form 7 January 2026; Accepted 31 January 2026
Available online 2 February 2026

performance of hydrological simulations. Subdaily simulations have generally been found to outperform daily simulations regarding global distribution metrics such as KGE (Kling-Gupta Efficiency) and RMSE (Brighenti et al., 2019; Huang et al., 2019; Lu et al., 2020; Li et al., 2020; Wang et al., 2015). However, they generally focus on a single hydroclimatic region or a single hydrological model. Furthermore, these studies do not explore the impact of time steps on specific hydrological metrics, such as mean flows, flood peaks and volumes, and events' seasonality. Yet, the overall performance of different conceptual hydrological model structures can be equivalent, while their internal behavior diverges (De Boer-Euser et al., 2017). Similarly, calibrating a hydrological model at different time steps could lead to similar overall performance but to distinct simulations at the event scale. It is therefore necessary not only to examine the impact of temporal resolution on various hydrological metrics, but also to investigate the underlying causes of the observed divergences between daily and subdaily simulations.

Existing publications that have examined specific hydrological metrics do not all agree on the impact of temporal resolution on the simulation of peak and average flows. According to Brighenti et al. (2019)'s review on Soil and Water Assessment Tool (SWAT) subdaily simulations, many studies suggest that subdaily modeling better represents daily peak flows, whereas daily modeling better captures average flows. However, this is not always the case: for example, Bastola and Misra (2013); Li et al. (2020) identified an added value of the subdaily resolution for both metrics. Similarly, Ficchì et al. (2016) found mixed results across a large set of 240 watersheds modeled with GR4 at different subdaily time steps in event mode. Half of the floods were insensitive to the time step, while about 25% were better simulated at subdaily temporal resolution. The greatest gain was obtained with the transition from 24-h to 12-h resolution. The remaining 25% of floods were better simulated at daily resolution. This substantial number of watersheds, for which refining the temporal resolution leads to a deterioration in model performance, contradicts the theoretical framework, which posits that a finer time step reduces numerical errors and improves model performance (Clark and Kavetski, 2010). However, the lower performance of the subdaily calibration is not necessarily attributable to the hydrological model only; it may also result from input data, whose uncertainty increases with finer temporal resolution. Markhali et al. (2022a) also observed divergences between daily and subdaily simulations on Québec watersheds simulated by two distributed hydrological models. They noted that these divergences appeared in validation, while the calibration metrics remained similar, the divergences being higher for the rarest floods and for convective seasons.

1.2. Reasons for differences between daily and subdaily simulations

Multiple studies have investigated how the choice of time step affects numerical errors in hydrological models with the following key findings: the numerical error associated with coarser time steps has been observed to increase with precipitation intensity (La Follette et al., 2021; Zhao et al., 2023); the numerical error depends on the discretization scheme employed in the hydrological equations, which is first-order for many widely used models, and leads to larger errors than higher-order discretization schemes (Clark and Kavetski, 2010; Zhao et al., 2023); parameters of conceptual hydrological models associated with slow processes exhibit stability with respect to temporal resolution, but parameters associated with quick processes reach stability only as the time step falls below the watershed characteristic time (Kavetski et al., 2011; Pan et al., 2021). Kavetski et al. (2011) further demonstrated using a small experimental watershed in Luxembourg, that hydrological parameters become more identifiable at finer time steps.

Direct runoff and coarse temporal discretization relative to the watershed's characteristic timescales are not the only factors contributing to differences between daily and subdaily simulations. For example, Li et al. (2020) conducted a comparative analysis of the simulations at hourly and daily time steps in a large watershed in Eastern Central China. The better performance of the hourly model was suggested to be related to a better representation of the routing to underground storage and the initial moisture conditions prior to the flood events. Bouaziz et al. (2021) also observed differences in storage filling and Fenicia et al. (2008) noted differences in the antecedent humidity conditions at different time steps. Meanwhile, Ficchì et al. (2019) and Fenicia et al. (2008) observed differences in interception behavior, while Bouaziz et al. (2021) reported variations in snow cover duration. Divergences in these internal variables are compensated by adjustments in other internal variables to match the observed outflows in calibration. However, as noted by Ficchì et al. (2019), the finer time step does not always provide a more accurate simulation of the internal variables. The systematic bias they observed in the simulated hourly interception compared to expected values from the literature led them to introduce a new parameter in GR4 to improve the representation of interception at the hourly time step (GR4H thus becoming GR5H). Finally, the findings of Astagneau et al. (2021) revealed that the same GR5H compensates both for differences between internal processes and for variations between seasons, especially between dry and wet periods.

Asadzadeh et al. (2016) propose an additional explanation for the effect of temporal resolution. They simulate flows in three watersheds in Southern Ontario, Canada, using the SWAT model. The results show that flood peaks resulting from end-of-day downpours in these watersheds were simulated on the same day as rainfall rather than the following day. This timing lag led to an underestimation of peak flood values. To correct this lag, they proposed a daily model calibration algorithm (SHIFT) to align the simulated peaks with observations.

Finally, although several recent studies have begun to run future simulations directly at subdaily time steps, few have compared the projections across different time steps. The results depend on the study configuration. Markhali et al. (2022b) identified strong interrelations between two distributed models applied in Québec watersheds and the spatial and temporal resolutions, which influenced the impact of climate change on flood metrics. In contrast, Beylich et al. (2021) found that the relative changes in return floods simulated by the semi-distributed HBV model for a group of German mountainous watersheds were independent of the temporal resolution.

1.3. Divergences between daily and subdaily future simulations

To further investigate the apparent contradictions between earlier studies, Destuynder (2025) simulated 221 watersheds considering diverse hydroclimatic contexts and seasons in Mexico, the United States and Québec (see Figure S.1 in the Supplementary Material) with two conceptual models (GR4H and MOHYSE). The 3- and 24-h calibrated models were driven by seven bias-corrected regional climate simulations. The impact of climate change on three flow metrics (seasonal mean, seasonal maxima, seasonal 100-year return flow) was compared between the daily simulations and the daily-averaged 3-h simulations. Temporal resolution and its interactions with hydrological models, reference climate datasets and climate simulations explained 0% to 74% of the variance in the computed changes, depending on watershed, season and flow metric, with an average of 19%.

The analysis revealed several notable trends. A larger part of the uncertainty was associated with temporal resolution 1) during the convective summer-fall season, 2) in the subregion encompassing Appalachia, Atlantic Coast and Québec, 3) for the more extreme floods, and 4) for the MOHYSE model. However, none of the regions and seasons exhibited a homogeneous pattern. For each region, season, model, and flood metric, roughly equal numbers of simulations produced larger changes under daily simulations as under daily-averaged 3-h simulations. In 11% of cases, changes in mean seasonal flow differed by at least 10% between daily and daily-averaged 3-h simulations. Changes in seasonal maxima differed between both time steps in 32% of simulations, and changes in 100-year return floods differed in 66% of the simulations (see Figure S.2 in the Supplementary Material). Moreover, in 6%, 9%, and 13% of

simulations, respectively, the changes in seasonal mean flow, seasonal maxima, and 100-year return floods showed opposing change directions between daily and daily-averaged 3-h simulations.

Building on five case studies from Destuynder (2025), this paper aims to address the following question: how do differences in temporal resolution interact with hydrological model structure and watershed characteristics to produce divergent or even opposite projected changes in key hydrological metrics across diverse hydroclimatic contexts?

Each case study refers to a different combination of watershed-hydroclimatic region-hydrological model. These specific case studies were selected because they encompass a good diversity of cases with opposite 3-h and 24-h projections.

2. Methods and materials

This section presents the full modeling chain that was applied to the 221 watersheds (Sections 2.1–2.4), before detailing the specific features of the five case studies highlighted in the present paper (Section 2.5). Details on each step of the entire modeling chain summarized here can be found in Destuynder (2025).

2.1. Calibration of the hydrological models

Destuynder (2025) calibrated two lumped conceptual hydrological models, GR4H (Perrin et al., 2003) and MOHYSE (Martel et al., 2025), on 221 North American watersheds with drainage areas ranging from 10 to 2007 km^2 (see Figure S.1 in the Supplementary Material). The watersheds were chosen from instantaneous hydrometric datasets of the following countries: USA (U.S. Geological Survey, 2021), Canada (Ministère de l'Environnement, de la Lutte contre les changements climatiques, de la Faune et des Parcs, 2020), and Mexico (Comisión Nacional del Agua, 2016; Comisión Federal de Electricidad, 2017), to cover a large range of hydroclimatic contexts, including snow-dominated, rain-dominated and mixed regimes. The calibration was performed at both 3- and 24-h time steps using precipitation and temperature as input data, and assuming that a gridded climate dataset adequately represents the historical climate. The observed daily flow series to match in the 24-h calibration were computed by averaging the observed 3-h flow series without gap-filling, to avoid biasing the calibration process. Two climate grids were used to calibrate the models over a 15-year period, covering each watershed's hottest years of the record: the reanalysis ERA5 (Hennermann, 2018, 30 km spatial resolution, 1 h), and the composite precipitation product MSWEP v2.8, hereafter called MSWEP2 (Beck et al., 2019, 0.1 ° spatial resolution, 3-h). Because MSWEP2 lacks temperature time series, the ERA5 temperatures were used for both calibrations. In total, eight automated calibrations were performed per watershed using the SCE-UA method of Duan et al. (1994) as the optimization algorithm and the KGE (Gupta et al., 2009) as the objective function: 2 hydrological models × 2 climate datasets × 2 time steps.

2.2. Reference and future climate simulations

Each of the calibrated models was then driven by regional climate simulations for a reference period (1979-2005) and a future period (2071-2100) corresponding to the RCP8.5 scenario. At the time of undertaking this research, seven regional climate simulations with a temporal resolution of 3-h or finer were available in North America (see Table S.1 in the Supplementary material for information about these seven simulations). The five cases analyzed in the present study correspond to four of these climate simulations, produced by the RegCM4 and CRCM5 regional climate models with a spatial resolution of 0.22 ° and a temporal resolution of 3-h, (see Table 2).

All precipitation and temperature time series were bias-corrected using the multivariate quantile mapping method of Cannon (2018). The climate gridded datasets (ERA5 or MSWEP2) used for calibration served as reference datasets for this bias correction. The climate change characteristics in each watershed for each season are described by usual metrics, such as the absolute difference between mean temperatures of the reference and future periods ($\Delta\overline{T}$); the relative difference between mean precipitations ($\Delta\overline{P}$), between maximum 3-h precipitations (ΔRX_3) and between maximum daily precipitations (ΔRX_{24}).

2.3. Computation of the flow metrics

After removing a one-year warm-up period, we computed the changes in flow metrics between the reference and the future periods for each simulation. These flow metrics were calculated at the seasonal scale to ensure the flood series they are based on is homogeneous. Up to four hydrological seasons were defined in each watershed by k-means clustering on historical peak-over-threshold flows: snowmelt season; winter-spring season associated with high base flow; summer-fall season associated with low base flow; fall-winter season associated with high base flow. We computed three flow metrics, namely seasonal mean flow $\overline{Q}^{(\Delta t)}$, seasonal maxima $\overline{Q^{(\Delta t)}_{AMS}}$, and 100-year return flood $Q^{(\Delta t)}_{100}$, for every simulation and time step in each season, and also on the full year.

Return floods were computed using two methods. First, a flood frequency analysis was performed on the seasonal maxima series (FFA-AMS), fitting the maxima series to the best-fitting distribution, according to the Anderson-Darling test (Anderson and Darling, 1954), from the following options: Bulletin 17C method (England Jr et al., 2019), Log-Pearson III, Gumbel and Generalized Extreme Values. Secondly, the best fit of the Peak-over-Threshold seasonal series to a Generalized Pareto distribution (FFA-POT) was chosen between Maximum Likelihood Estimation method (MLE), and Method of Moments (MOM). Changes in the flow metrics were computed for each watershed, simulation and time step, as the relative differences between reference (r) and future (f) periods. For instance, the change in the mean seasonal flow is: $\Delta\overline{Q} = 100\left(\overline{Q}_f^{(\Delta t)} - \overline{Q}_r^{(\Delta t)}\right)/\overline{Q}_r^{(\Delta t)}$.

2.4. Overview of the hydrological models

MOHYSE is a ten-parameter lumped conceptual model. It employs three stores representing the snow cover, the unsaturated zone and the saturated zone, and allows water exchanges between the river, the unsaturated zone and the aquifer. The final water depth resulting from these exchanges is routed to the outlet through a Nash unit hydrograph. MOHYSE's internal equations are identical for both time steps.

GR4H is a widely used lumped conceptual model with four-parameters. It is based on two independent stores (production and routing) and two intermediate unit hydrographs. It also allows inter-catchment groundwater exchanges. GR4H was coupled with the CEMANEIGE snow module (Valéry, 2010) to simulate snow accumulation and melting. The GR4H structure was adapted to the time step following the recommendations of Mathevet (2005); Le Moine (2008). SH_{exp}, the exponent of the unit hydrograph function, is time-dependent in order to achieve consistency between the 24-h and the daily-averaged 3-h discretized unit hydrographs computed with the same time base x_4. Time-dependent coefficients are also included in the formulations of the percolation $Perc_t$, the groundwater exchanges F_t and the output flow from the routing store Q_{r_t}. The snow accumulation and melting were computed with CEMANEIGE at the daily time step depending on the minimum and maximum daily temperatures, and then disaggregated at the 3-h time step using the parabolic scheme of Parton and Logan (1981). The formulation of net rainfall and evapotranspiration (P_{n_t}, E_{n_t}, P_{s_t}, E_{s_t}) remains the same for both time steps.

Details on the definition and calculation of each internal variable are provided for each hydrological model in Appendices A (MOHYSE) and B (GR4H).

2.5. The case studies

The five case studies presented in this paper were selected from the total of 2704 simulations generated in Destuynder (2025). These cases were selected among the watersheds showing strong divergences in projected flow metric changes between daily and 324 simulations.

Table 1
Characteristics of the watersheds in the five case studies.

Watershed name	Region	Area	Time of concentration (Bransby Williams, 1922)	Hydrological regime
Morpions	Québec (Canada)	94 km^2	8.3 h	Mixed
Tzimbas	Chiapas (Mexico)	124 km^2	10.8 h	Rain
Sipsey Fork	Alabama (USA)	238 km^2	11.1 h	Rain
Zahuapan	Puebla (Mexico)	1105 km^2	21.7 h	Rain
War Eagle Creek	Arkansas (USA)	688 km^2	31.8 h	Rain

Table 2
Simulations characteristics.

Watershed name	Hydrological model	Historical climate dataset	Regional climate simulation	Calibration KGE			Section	Studied divergence
				$KGE_c^{(24)}$	$KGE_c^{(3)}$	$KGE_c^{(324)}$		
Morpions	MOHYSE	ERA5	MPI - RegCM4	0.71	0.73	0.75	3.1.1	Floods
Tzimbas	GR4H	MSWEP-V2	HadGEM - RegCM4	0.76	0.62	0.74	3.1.2	Floods
Sipsey Fork	GR4H	ERA5	HadGEM - RegCM4	0.63	0.66	0.69	3.1.3	Floods
Zahuapan	GR4H	MSWEP-V2	CNRM - CRCM5	0.51	0.58	0.50	3.2.1	Hydrograph
War Eagle Creek	MOHYSE	ERA5	CanESM2 - CRCM5	0.67	0.67	0.71	3.2.2	Floods

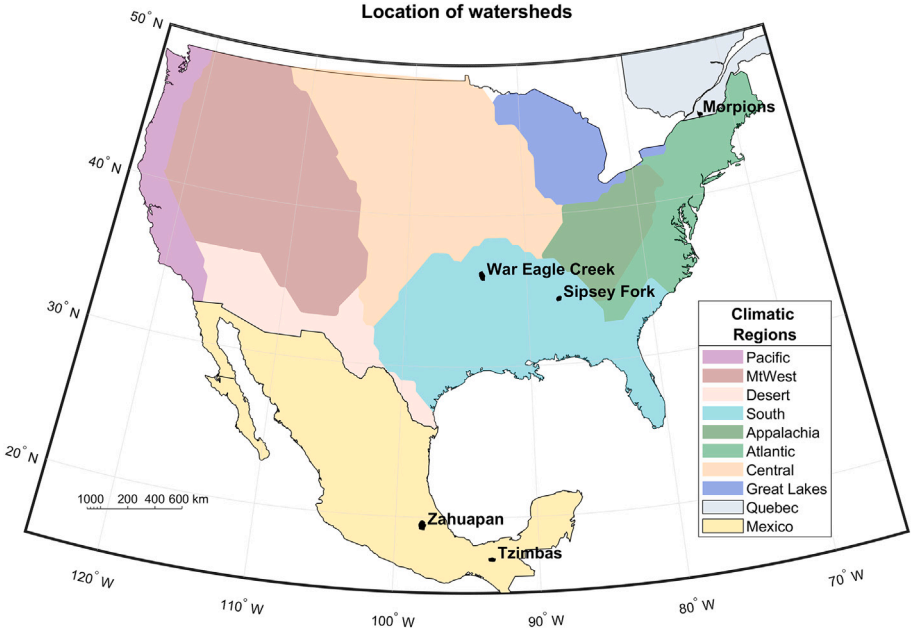

Fig. 1. Location of the five watersheds. The climate classification is adapted from Bukovsky (2012).

The selection includes: both GR4H and MOHYSE simulations; both rain-dominated and mixed rain/snow regimes; opposite change projections of daily and 324 simulations on both annual hydrographs and floods. The characteristics of the five selected watersheds are presented in Table 1, and the configuration of their simulations in Table 2. A map showing the watersheds is provided in Fig. 1.

2.6. Comparison of the simulations

To investigate the causes of divergence between the daily and sub-daily simulations, we primarily compared the internal variables of the hydrological models. More precisely, comparisons were made among the following four simulation types, depending on the needs of each case study. Their characteristics are synthesized in Table 3.

- Time series extracted from the daily simulations, run with the parameter set calibrated at the daily time step, $x^{(24)}$.
- Time series extracted from the 3-h simulations, run with the parameter set calibrated at the 3-h time step, $x^{(3)}$.
- Daily-averaged time series extracted from the 3-h simulations, also run with $x^{(3)}$. These time series are referred to as 324 simulations.
- Time series extracted from daily simulations run with a parameter set called $x^{(24t)}$, constructed by transferring the $x^{(3)}$ parameter set to the daily scale. These time series are referred to as 24t simulations. The transfer procedure is detailed in Appendix C. For MOHYSE, coefficients representing a flow per unit of time are simply linearly scaled. The parameters of the 24t Nash unit hydrograph, are chosen to ensure an identical time-to-peak of the 3-h and 24t unit hydrographs. For GR4H, consistency between the parameter sets at both time steps is internally ensured within the model, so the only adjustment needed is the conversion of the 3-h calibrated time base $x_4^{(3)}$ to daily units to obtain $x_4^{(24t)}$.

Internal variables extracted from a given simulation are specified in a superscript. For example, $P_{n_t}^{(24)}$, $P_{n_t}^{(324)}$, $P_{n_t}^{24t}$ denote GR4H net precipitation computed in the 24, 324, and 24t simulations respectively, while P_{n_t} refers to the general formulation valid across all types of simulations.

Table 3
Designation of the simulations employed to compute the flow metrics.

Name	Parameter set	Parameter set construction	Time step of the run	Daily-averaging of the flow time series
3-h	$x^{(3)}$	Calibration	3-h	No
324	$x^{(3)}$	Calibration	3-h	Yes
24t	$x^{(24t)}$	Transferred from $x^{(3)}$ (see Appendix C)	24-h	–
24-h	$x^{(24)}$	Calibration	24-h	–

Comparing simulations 324 and 24t allows us to isolate the exact impact of the discretization time step on the numerical resolution of the equations, since their parameter sets are equivalent. This comparison complements that of the 324 and 24-h simulations. In the latter case, the discretization errors of the coarser daily model are compensated for by the $x^{(24)}$ parameter set, which differs from the 3-h one. In future climate simulations, the comparison between 324 and 24-h helps assess how these compensations behave under climate conditions that differ from those used for calibration. Conversely, the comparison between 324 and 24t allows us to determine whether discretization errors themselves vary with climate, both at the event scale and over the long term.

3. Results

The results are organized into five case studies, each presenting the divergences observed between 3-h and 24-h projections and analyzing their causes. The first three cases illustrate possible responses of the hydrological models to the loss of information in high-frequency inputs at the daily time step, and are grouped in Section 3.1. The last two cases analyze the consequences of time-step dependency in the discretization of nonlinear equations and are grouped in Section 3.2.

3.1. Cases involving high-frequency hydroclimatic information

3.1.1. Morpions watershed: filtering of the snowmelt diurnal cycle (MOHYSE)

This case study investigates the impact of time step on the simulation of snowpack and snowmelt by MOHYSE in the 94 km^2 Morpions watershed in Québec. Morpions is a watershed characterized by a mixed hydrological regime, exhibiting annual maxima resulting from both snowmelt and summer-fall rain events. The 3-h and 24-h configurations demonstrate similar calibration performance (KGE values are 0.73 and 0.71, respectively; not shown).

• *Lower melting threshold and slower melting in daily calibrations.* Both configurations simulate similar March snowmelt dynamic processes, as illustrated in Fig. 2. However, the 24t model simulates a higher annual peak snow storage than the 324 model—167 mm versus 113 mm (see Figures S.3a and S.3c in the Supplementary Material). By accounting for the diurnal temperature cycle, the 3-h simulation initiates melt during the warmest hours of the day, leading to earlier, more frequent melt events (68 vs. 42 melt days per year), but of lower intensity than those in the 24t simulation using the equivalent $x^{(24t)}$ parameter set. The 3-h modeled snowmelt thereby aligns more closely with observed physical processes. To compensate for the lack of a diurnal cycle and to enable sufficient snowmelt, the 24-h calibration results in a lower melt threshold temperature than the 3-h model ($T_f^{(24)} = -5\,°C$ versus $T_f^{(3)} = 0.6\,°C$, see Table S.2 in the Supplementary Material).

With this lower melt threshold, the maximum snow storage level for this case study becomes equivalent to that computed in the 324 simulation (118 mm on average in the reference period; see Figure S.3b in the Supplementary Material). The 24-h model shows a greater number of snowmelt days (on average 81 days per year). To maintain calibration accuracy and avoid generating unrealistic floods when the temperature is between −5°C and 0°C, the 24-h calibration also demonstrates a lower melt coefficient than the 3-h model. Both compensatory adjustments (lower melt threshold and melt coefficient at the 24-h time step with MOHYSE) are observed across most of the snow-covered watersheds in the complete sample of 221 watersheds. As a result, the snowmelt flood peaks are lower in the 24-h simulation than in the 324 simulation (see Fig. 2(c), and the annual maximum occurs more frequently during the snowmelt season in the 324 simulation than in the 24-h version—particularly in future simulations (see Fig. 2(b)).

• *Adaptation of daily and subdaily models to winter-spring climate change.* The divergence in the internal snowmelt processes between the 324 and 24-h simulations causes distinct adaptations of each version to climate change. The 324 model projects an increase in rare flood discharges

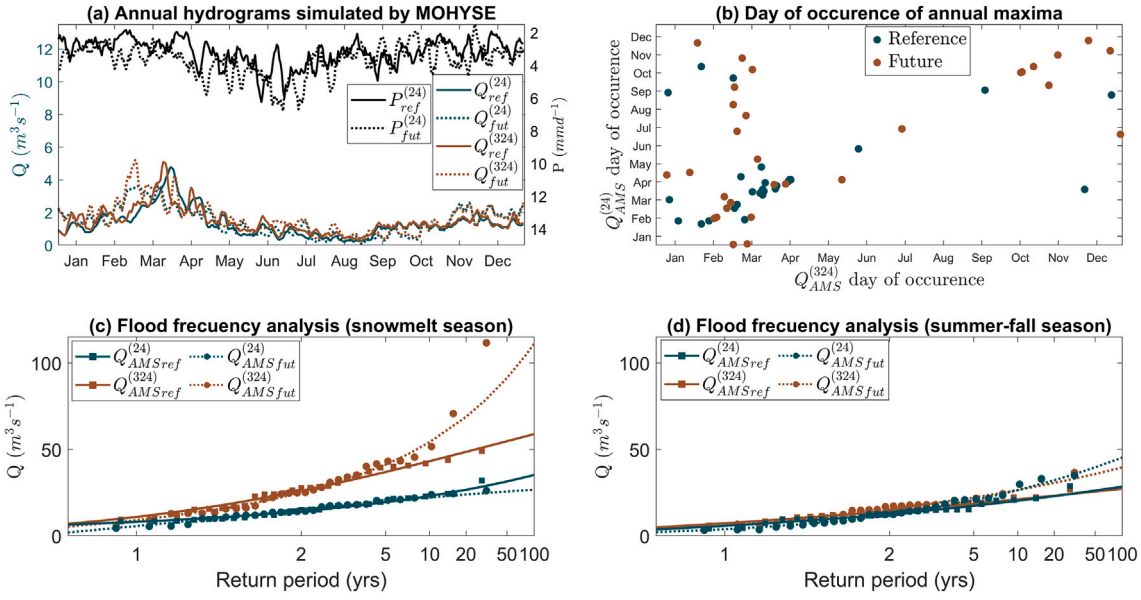

Fig. 2. Example of opposing climate change signals on the snow-covered Morpions watershed simulated with MOHYSE. (a): Mean annual hydrographs and hyetographs for the reference and future periods. (b): Occurrence day of the annual maxima. (c): flood frequency analysis in the reference/future climates (GEV distribution) for the snowmelt months (January to April). (d): Same as (c) for May to December. Uncertainty margins on the return flows are not shown to improve readability.

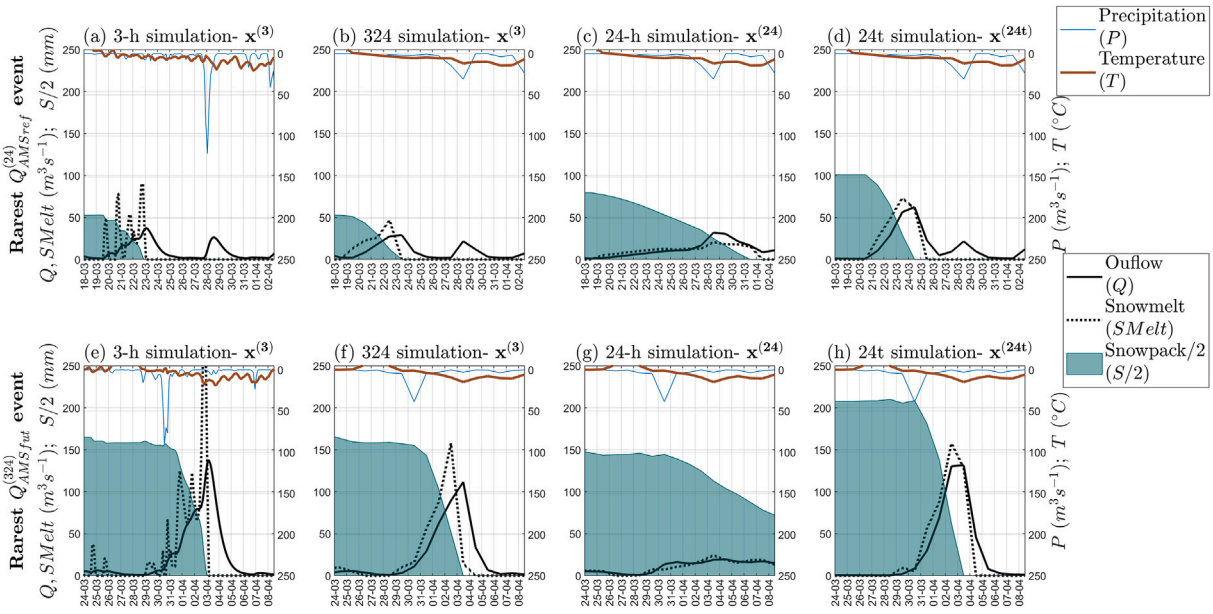

Fig. 3. Morpions watershed: Simulation of two rare flood events in the reference and future periods. Most extreme floods from the reference and future time series are simulated: at 3-h (a, e); at 324 (b, f); at 24-h (c, g); and at 24t (d, h). The temperature and incoming raw precipitation are shown on the upper x-axis, while the lower axis represents the snow storage level (mm/2), the snowmelt ($m^3\ s^{-1}$) and the outflow ($m^3\ s^{-1}$).

during the snowmelt season ($\Delta Q^{(324)}_{100} = 92\%$), whereas the 24-h model exhibits a decrease ($\Delta Q^{(24)}_{100} = -26\%$, see Fig. 2(c). The projected climate change in this simulation is characterized by a 24% increase in winter precipitation volumes. Consequently, the future rare floods occur during high winter-precipitation years leading to increased maximum snow storage at levels not observed in the past (see Figures S.3d to S.3f in the Supplementary Material). At the end of the season, the rapid melt coefficient in the 324 simulation produces a higher peak than historical levels, while the 24-h model distributes snowmelt over several episodes. An analysis of the precipitation time series shows that these exceptional years result from a higher intensity of winter precipitation rather than an increased frequency of snowy days (figure not shown).

Differences among the 324, 24t and 24-h versions can be observed in Fig. 3, which displays the rarest event of the 24-h AMS series in the reference period (top row) and the rarest event of the 324 AMS series in the future period (bottom row). In this figure, the following processes can be observed: the diurnal snowmelt cycle simulated at 3-h (Fig. 3(a) and (e)); the swelling of snow storage simulated with the 24t parameter set, and its consecutively overestimated snowmelt peaks compared to 324 (Fig. 3(d) and (h)); the similar storage heights obtained with the 324 and the 24-h calibrated models (Fig. 3(b) and (c)); and the damping of 24-h snowmelt peaks compared to the 324 simulation (Fig. 3(c) and (g)).

It is noteworthy that the rarest floods in both the reference and future periods correspond to the final snowmelt flood in spring, and that the damping of snowmelt in the 24-h calibrated simulation can lead either to 24-h floods that are higher than the 324 floods (top row) or vice versa (bottom row). In the reference rarest event, the higher 24-h flood peak (32 $m^3\ s^{-1}$) on March 28 results from the conjunction of a rainfall event with the last snowmelt of the year (Fig. 3(c)), while the 324 event (22 $m^3\ s^{-1}$) is a flood driven solely by rainfall, as the snowpack had already totally melted by March 23 (Fig. 3(b)). In the future event, the higher 324 flood (112 $m^3\ s^{-1}$) is the one that reflects the mix of both rainfall and the last snowmelt of the year (Fig. 3(f)), while the 24-h simulation (19 $m^3\ s^{-1}$) results in its habitual smoothed snowmelt (Fig. 3(g)).

3.1.2. Tzimbas watershed: filtering of short-duration rainfall (GR4H)

The previous case study addressed differences between 324 and 24-h projections arising from the adaptation of the 24-h parameter set to compensate for the filtering of cyclic subdaily processes like the diurnal snowmelt cycle. Filtering at daily time steps can also occur at the event scale, with a low impact on the parameter sets during the calibration process, but a high impact on the computation of the flood metrics. Fig. 4 shows a case in which the hydrological model projects a strong decrease in the 3-h 100-year return flows (– 41%, Fig. 4(d)) and a slight increase in the 324 (+1%, Fig. 4(e)) and 24-h (+2%, Fig. 4(f) 100-year return flows. The opposition is also visible in the annual maxima changes: the simulation projects a decrease of 13% of $\overline{Q^{(3)}_{AMS}}$ but an increase of respectively 8% and 3% of $\overline{Q^{(324)}_{AMS}}$ and $\overline{Q^{(24)}_{AMS}}$ (Fig. 4(c)).

The reference streamflow time series displays a rare flood peak, which is significantly higher in the 3-h time series than in the daily-averaged (324) time series (Fig. 4(a)). This outlier skews the annual maxima series, yielding a mean that is notably higher than the median (Fig. 4(c)), and it also forces an adjustment toward a heavy-tailed statistical distribution (Fig. 4(d)). Since the future time series does not contain such a rare event, a decrease in the 100-year flood metric is observed from the 3-h simulations. By trimming the outlier, the past and future flood series are relatively similar, as in the 324 and 24-h flood series (Fig. 4(e) and (f)), where the reference outlier is absent.

Figure S.4 in the Supplementary Material illustrates the zoomed version of the event and the associated hydrographs produced at 3-h, 324, and 24-h simulations (Figure S.4a, S.4b, S.4c, respectively). The comparison of the three simulations shows that the 324 and 24-h versions are similarly unable to capture the intensity of this rainfall event characterized by a 194 mm depth in 6 h. Daily-averaging the subsequent 3-h flood peak of 947 $m^3\ s^{-1}$ damps the peak to 275 $m^3\ s^{-1}$, corresponding to a very high peak factor ratio of 3.4 between the 3-h peak and the 324 peak. An analysis of the climate reference time series indicates that this outlier is associated with an exceptionally intense rainfall event recorded in the historical time series of the MSWEP2 reference climate dataset. The MSWEP2-based bias correction applied to the climate simulations for the reference period increases the magnitude of the most

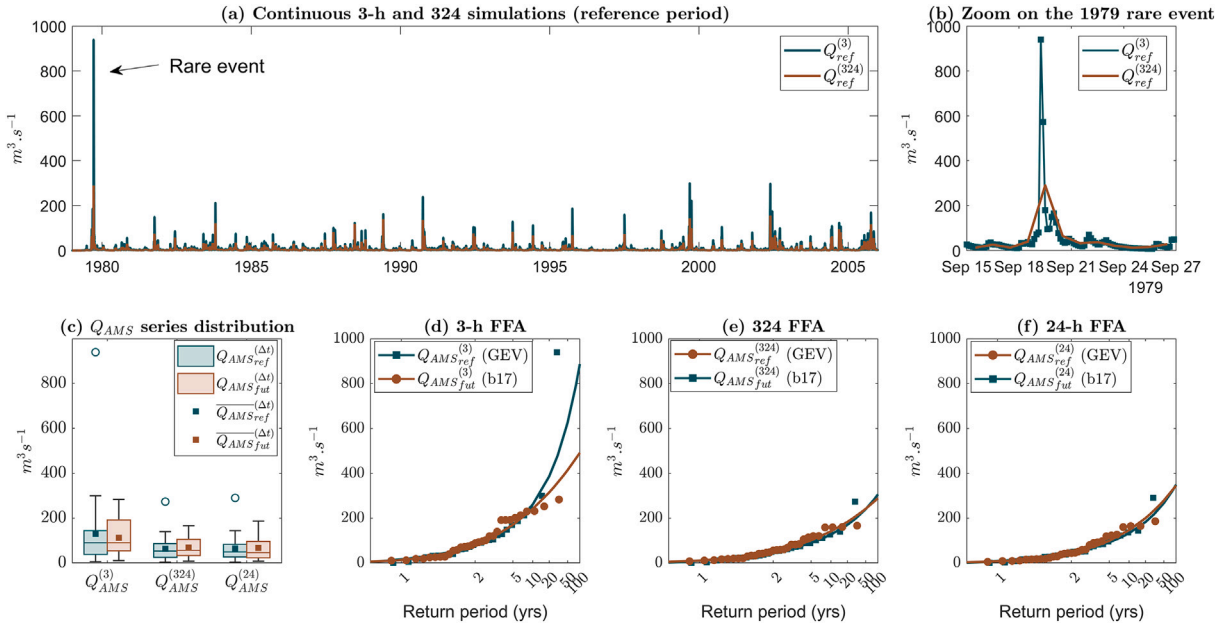

Fig. 4. Example of the filtering of short rainfall event in the Tzimbas watershed. (a) Continuous 3-h and 324 simulations over the entire reference period, and (b) zoom on the rare event. (c) Boxplot of the annual maxima from the 3-h, 324, and 24-h time series. The mean values of the AMS series ($\overline{Q_{AMS}}$) are indicated by squares. (d), (e), and (f): annual FFA-AMS of the 3-h, 324, and 24-h time series.

extreme event in each climate simulation for this watershed, resulting in consistent behavior across both hydrological models and all climate simulations. Although automatic weather station data are not available in this mountainous Chiapas watershed to confirm the plausibility of the MSWEP2 event, its magnitude is comparable to the intense, rare storms observed at other stations in the region.

3.1.3. Sipsey fork watershed: impact of the positioning of the 24-h window relative to the event timing (GR4H)

Section 3.2.2 demonstrated how the timing of 3-h flood peaks within the 24-h window can affect the 324 flood peak values. The following is a more detailed example of a 237 km^2 Alabama watershed, showing that this impact previously observed at the event scale has consequences at the climatic scale. The daily version of GR4H was driven by the reference and future climate simulations that were daily-aggregated using the Universal Time Coordinates (UTC) on one side, and the Local Standard Time (LST) on the other side (UTC-6 on this watershed). The same set of hydrological parameters, calibrated in UTC time, was used for both simulations for comparison purposes. The 3-h simulation was also aggregated to calculate the 324 time series, both with the UTC and the LST windows. Figure S.5 displays a hydrological season of the future simulations, as an example of the chosen time of reference's impact on the flood peaks. It impacts both the 24-h and the 324 simulations, resulting in peaks sometimes higher in UTC, and sometimes higher in LST, depending on the timing of the events. LST peak values vary between -40% and $+40\%$ from the UTC peak values, whether they are computed based on the 24-h or the 324 time series. Also, LST and UTC peaks do not always occur on the same day. 21% percent of future UTC peaks are delayed by one day compared to LST peaks while 1% are advanced, whether they come from the 24-h or the 324 time series. In the 324 time series, this delay corresponds to 3-h peaks occurring at the end of the day in LST time, and at the beginning of the next day in UTC time.

Fig. 5 shows an example of the differences in the simulation of a major event in UTC time (a) and LST time (b), at the 324 and 24-h time steps. This future 33-h long clustered rainfall event peaks in the time slot 0 h-3 h on March 12, 2080 in UTC time (Fig. 5(a)), leading to a flood peak of 159 m^3 s^{-1} during the 6 h-9 h interval. Most of the flood volume therefore discharges at the outlet during March 12, leading to a relatively high 324 peak of 105 m^3 s^{-1} on this day. However, when the 3-h time series is converted to LST time, the 3-h flood peak occurs during the 0 h-3 h interval, spreading the flood volume between March 11 and March 12 and lowering the 324 peak to 75 m^3 s^{-1} (Fig. 5(b)). In contrast, the UTC time spreads the rainfall volume between March 11 and March 12 while its main part is concentrated during March 11 only in LST time. This results in a high 24-h peak on March 11 in LST time (Fig. 5(b)), 106 m^3 s^{-1}) but a smoothed flood spread over two days in UTC time (Fig. 5(a)), 67 m^3 s^{-1}). The relative behaviors of 324 and 24-h time series at UTC and LST times are therefore opposite for this event.

This is not an isolated case: Fig. 6 compares the AMS at UTC and LST times, for 324 and 24-h time series, during reference and future periods, in the same watershed. During the reference periods, 324 LST peaks tend to be higher than UTC ones, while 24-h UTC peaks tend to be higher than 24-h LST peaks. Conversely, during the future period, 324 LST peaks and 24-h UTC peaks tend to be higher. This characteristic is particularly visible in 324 time series. As a consequence, climate change signals on flood metrics are opposite in LST and UTC: UTC time projects an increase in the magnitude of 324 floods ($\Delta\overline{Q_{AMS}^{(324)}} = 8\%$, $\Delta Q_{100}^{(324)} = 24\%$) while LST time projects a decrease ($\Delta\overline{Q_{AMS}^{(324)}} = -3\%$, $\Delta Q_{100}^{(324)} = -14\%$). On the contrary, UTC time reference projects a slight decrease in the magnitude of 24-h annual maxima ($\Delta\overline{Q_{AMS}^{(24)}} = -4\%$) while LST time projects a slight increase ($\Delta\overline{Q_{AMS}^{(24)}} = 2\%$). Both UTC and LST times project a decrease in 100-yr floods ($\Delta Q_{100}^{(24)} = -13\%$).

These opposite projections in LST and UTC time are connected to a shift and an intensification of the future diurnal cycle of the precipitation: one third of the events of the future 3-h annual maxima series are due to a peak of rainfall during the 15 h-18 h time slot (LST), i.e., during the 21 h-24 h time slot (UTC). The $x_4^{(3)} = 14$ h time-to-peak of the calibrated unit hydrograph routes these events into floods peaking during the 3 h-6 h intervals (LST), i.e., 9 h-12 h (UTC). Consequently, the future 324 LST floods tend to be lower than the future 324 UTC floods because

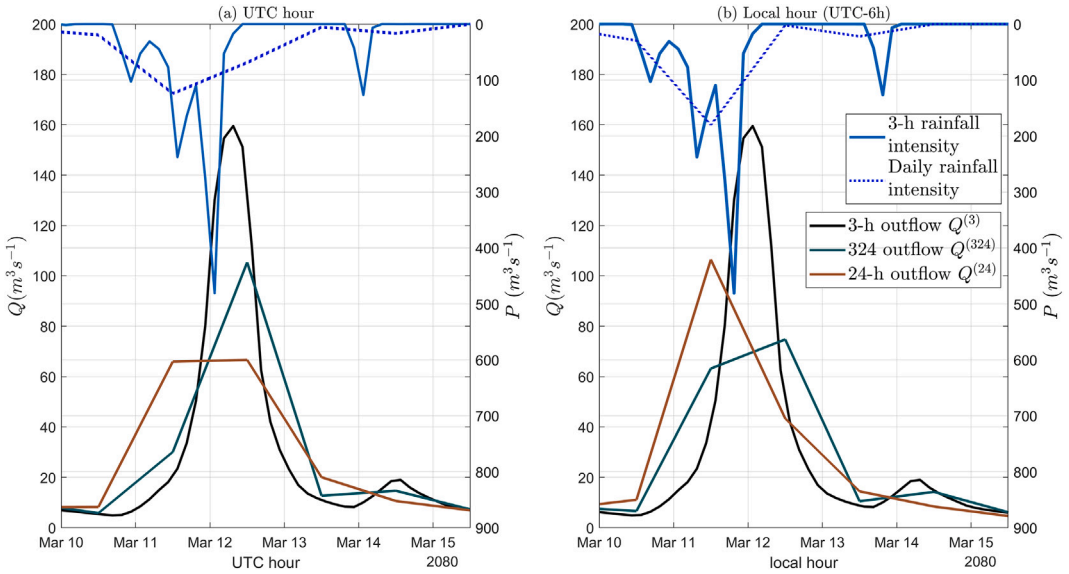

Fig. 5. Simulation of a 36-h rainfall event on the Sipsey Fork river watershed in (a) UTC time, vs. (b) LST time (UTC-6 h). Upper x-axes show the mean rainfall intensity at the time step scale. Lower x-axes show the simulations at 3-h, 324 and 24-h time steps. The parameter sets were calibrated in UTC time. UTC and LST simulations are obtained by forcing the models with UTC and LST climate time series using the same parameter set.

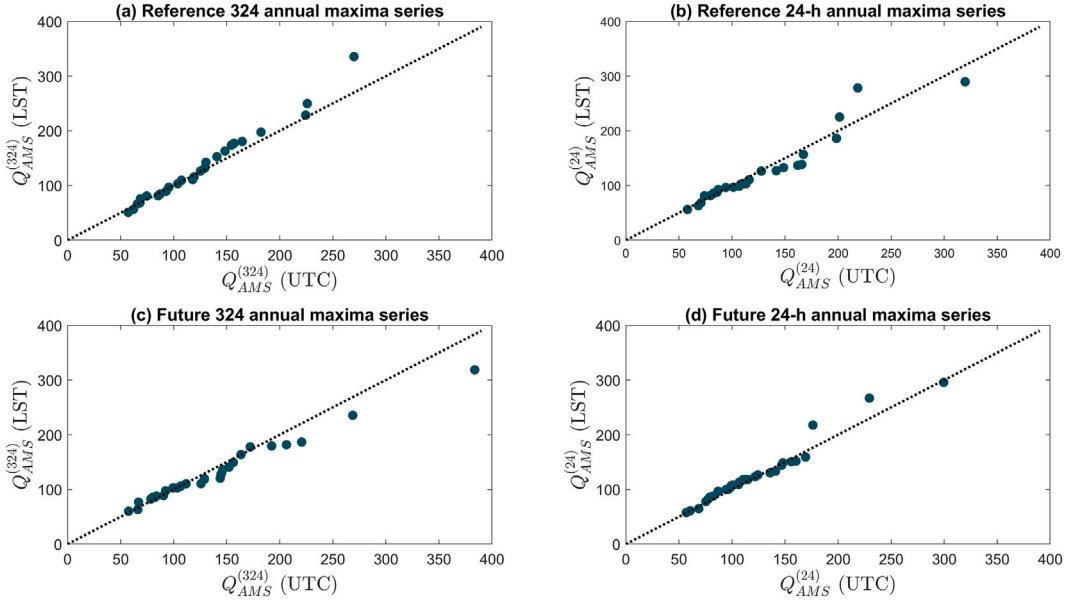

Fig. 6. Sipsey Fork river watershed: QQ-plots of LST vs. UTC annual maxima series, for reference (a, b) and future (c, d) simulations, at 324 and 24-h time steps.

they are more often spread over two days. A similar reasoning can be applied to the 24-h time series to explain the opposite climate change signal between LST and UTC simulations.

3.2. Cases related to discretization of nonlinear equations

3.2.1. Zahuapan watershed: time-step dependent solving of nonlinear equations (GR4H)

Fig. 7 shows a GR4H divergence case between the hydrograph projections at 24-h (Fig. 7(a)) and at 324 (Fig. 7(b)) for the high-altitude Zahuapan watershed in central Mexico. The climate simulation projects an increase in precipitation volumes during the September–October rainfall season. In the 324 simulation, the projected hydrograph follows the projected hyetograph (correlation of 0.8), with an 18% increase in annual $\overline{Q^{(324)}_{AMS}}$ (Fig. 7(b)). In contrast, the projected 24-h hydrograph (Fig. 7(a)) does not respond to such an increase (correlation of 0.67), and shows a 32% reduction in annual $\overline{Q^{(24)}_{AMS}}$.

The contrast between the projected 324 and 24-h hydrographs stems from differences in their production storage capacities. The 24 h-calibrated production storage capacity (x_1 in GR4H) is more than four times larger than the 3-h-calibrated capacity (see Table S.3 in the Supplementary Material). Since the relationship between the storage levels of different capacities follows a hysteresis curve (Eq. B.8), these different capacities result in a higher variability for the 3-h storage level: the 3-h (and thus the 324) storage level fills faster at the beginning of the rainfall season than that of the 24-h, reaches a higher peak, and declines faster. Fig. 8 shows the mean annual variation of GR4H internal

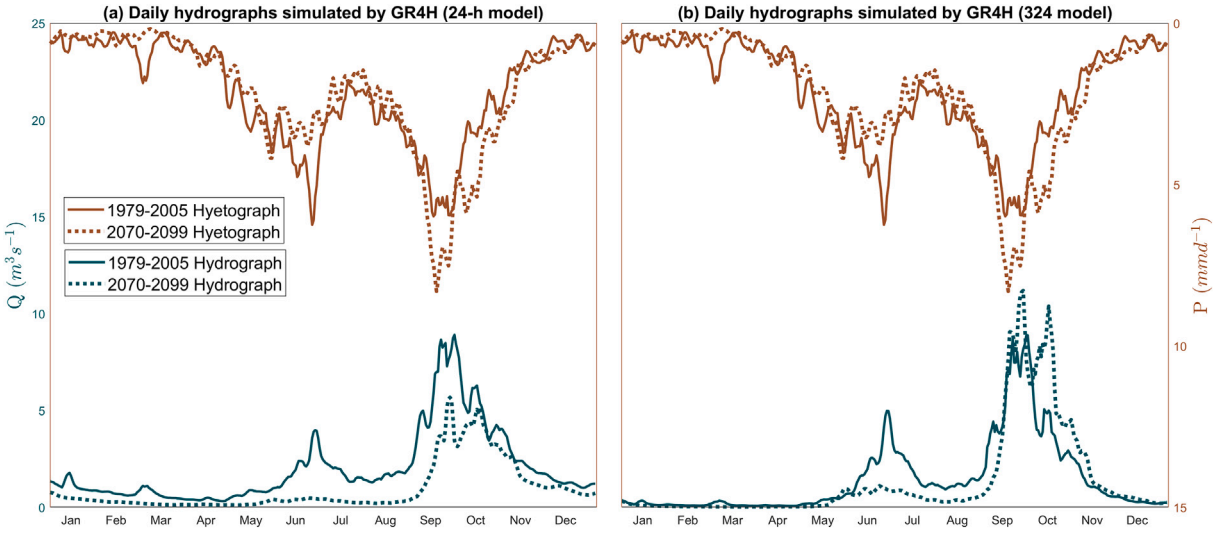

Fig. 7. Example of an opposite climate change signal on the annual hydrograph in the Zahuapan watershed. The mean annual hydrographs and hyetographs for the reference and future periods are plotted from GR4H simulations at 24-h (a) and 324 (b). The annual hydrographs and hyetographs are smoothed using a 5-day moving average.

variables, at 24-h, 324, and 24t, during the reference and future periods. The higher sensitivity of the 324 (with respect to 24-h) due to the smaller production store can be seen in Fig. 8(c). Due to the projected decrease in mean precipitation, the mean annual storage level decreases from 46% to 35% in both simulations. However, the rapid filling of the 324 storage, combined with the September-October precipitation increase, leads to a slightly delayed and higher 324 annual maximal storage level compared to the reference level, in contrast to the decreased annual maximum level observed in the 24-h simulation. As a consequence, the precipitation entering the 324 production storage, $P_{s_t}^{(324)}$, is lower than $P_{s_t}^{(24)}$ during the fall season (Fig. 8(d)), while the water evaporated from the storage, $E_{s_t}^{324}$, is higher than $E_{s_t}^{(24)}$ (Fig. 8(e)). Thus, the 324 available water for runoff ($P_{n_t}^{(324)} - P_{s_t}^{(324)}$) is higher than in the 24-h simulation (Fig. 8(h)).

Fall filling levels also explain why $P_{n_t}^{(324)} - P_{s_t}^{(324)}$ is higher in the future period than in the reference period, whereas $P_{n_t}^{(24)} - P_{s_t}^{(24)}$ is lower. Including the percolation flow does not alter this result (figure not shown). However, accounting for losses due to water exchanges reduces the difference between the fall maxima in the 324 and 24-h simulations (Fig. 8(j)), because the water exchange parameter x_2 is three times more negative at the 3-h time step (Table S.3 in the Supplementary Material). Routing through the routing storage has no effect on the difference on an annual scale, since its capacity is nearly identical at both time steps (Fig. 8(i)).

Multiple calibration efforts at both 24-h and 3-h time steps consistently produced similar 4:1 ratios between production storage capacities $x_1^{(24)}$ and $x_1^{(3)}$. Losses characterized by x_2 were also consistently higher for the 3-h time step. Therefore, the difference noted between $x_1^{(24)}$ and $x_1^{(3)}$ in the initial calibration cannot be attributed to a numerical manifestation of equifinality. It stems instead from the nonlinearity of the logical condition used to compute P_{n_t} and E_{n_t} (Eqs. (B.6), and Fig. 8(a) and (b)).

• *Impact of discretization time step on water balance.* Let us assume that a day u is divided into two sets: D, a set of dry 3-h time steps ($P_t^{(3)} < E_t^{(3)}$), and R, a set of rainy 3-h time steps ($P_t^{(3)} > E_t^{(3)}$). The daily net precipitation and evapotranspiration can be compared for the 24-h and the 324 simulations depending on the sign of the daily precipitation minus potential evapotranspiration budget:

During a rainy day ($P_u^{(24)} > E_u^{(24)}$):

$$\text{At 324:} \begin{cases} E_{n_u}^{(324)} = \sum_{t\in D} \left(E_t^{(3)} - P_t^{(3)}\right) \\ P_{n_u}^{(324)} = \sum_{t\in R} \left(P_t^{(3)} - E_t^{(3)}\right) \end{cases} \tag{1}$$

$$\text{At 24-h:} \begin{cases} E_{n_u}^{(24)} = 0 & < E_{n_u}^{(324)} \text{if } D \neq \varnothing \\ P_{n_u}^{(24)} = \sum_{t\in\{R,D\}} \left(P_t^{(3)} - E_t^{(3)}\right) & \\ P_{n_u}^{(24)} = P_{n_u}^{(324)} - E_{n_u}^{(324)} & < P_{n_u}^{(324)} \text{if } D \neq \varnothing \end{cases} \tag{2}$$

During a dry day ($P_u^{(24)} < E_u^{(24)}$):

$$\text{At 324:} \begin{cases} E_{n_u}^{(324)} = \sum_{t\in D} \left(E_t^{(3)} - P_t^{(3)}\right) \\ P_{n_u}^{(324)} = \sum_{t\in R} \left(P_t^{(3)} - E_t^{(3)}\right) \end{cases} \tag{3}$$

$$\text{At 24-h:} \begin{cases} E_{n_u}^{(24)} = \sum_{t\in\{R,D\}} \left(E_t^{(3)} - P_t^{(3)}\right) & \\ E_{n_u}^{(24)} = E_{n_u}^{(324)} - P_{n_u}^{(324)} & < E_{n_u}^{(324)} \text{if } R \neq \varnothing \\ P_{n_u}^{(24)} = 0 & < P_{n_u}^{(324)} \text{if } R \neq \varnothing \end{cases} \tag{4}$$

In both cases, the 324 approach yields higher daily net precipitation and net evapotranspiration, as soon as the day is composed of rainy and dry time steps. 24-h and 24t are interchangeable in this context, as the computation of the net precipitation does not depend on any calibrated parameters. In the reference period, 28% of $E_{n_t}^{(24)}$ values are zero while $E_{n_t}^{(324)}$ is nonzero—corresponding to lower $P_{n_t}^{(24)}$ than $P_{n_t}^{(324)}$—and this share declines to 24% in the future period due to fewer rainy days. As a consequence, the total annual net precipitation at the 24-h time step ranges from 42% to 68% of that at the 324 time step depending on the year, with a mean of 60%. The projected annual evapotranspiration capacity at the 24-h time step is on average 69% of the 324 time step. These divergences exhibit a clear seasonal pattern driven by rainfall characteristics, and become most pronounced during the convective season. For this watershed, Fig. 8(a) shows that $P_{n_t}^{(24)}$ is mostly lower than $P_{n_t}^{(324)}$ during the first rainfall season, which is characterized by short-duration

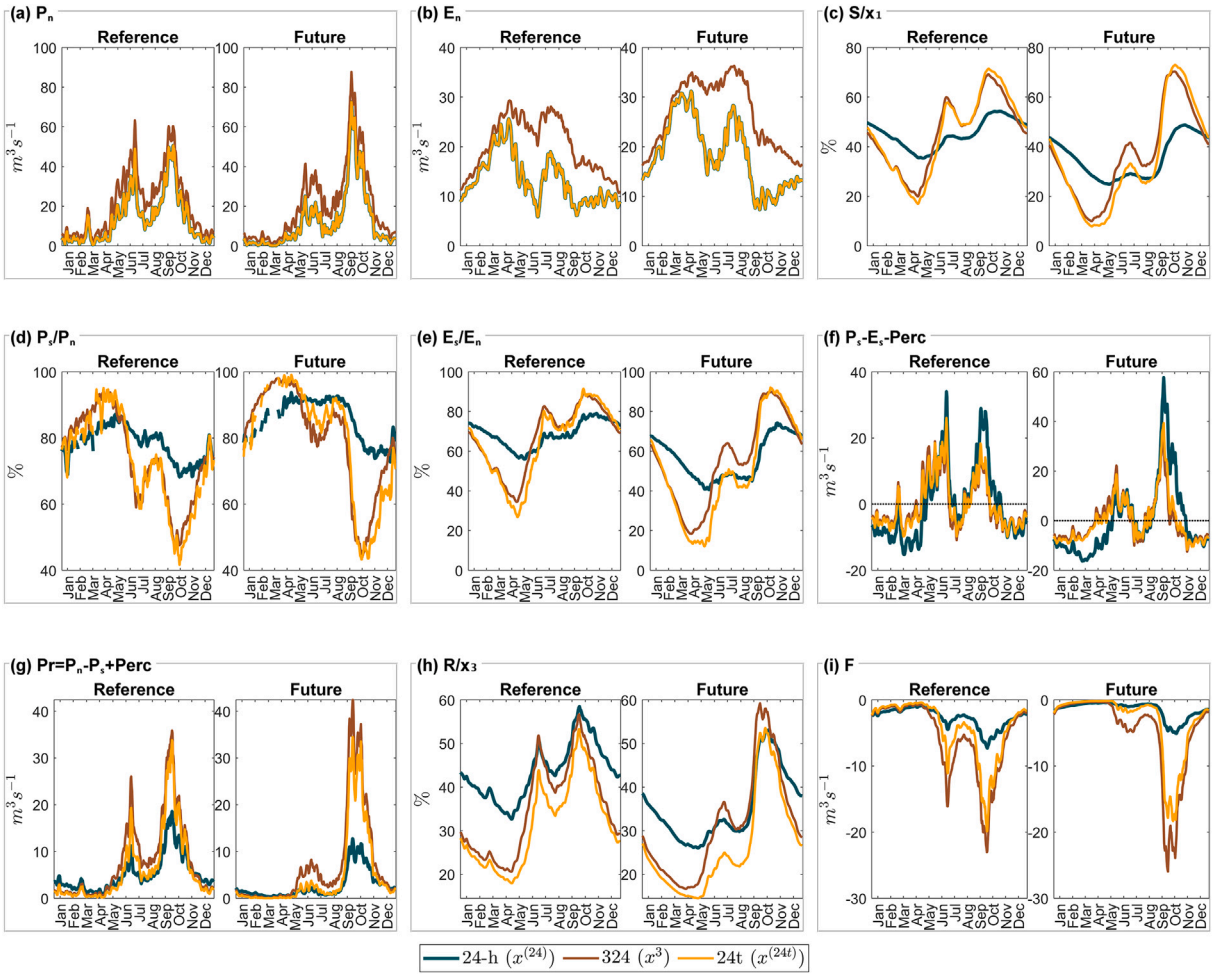

Fig. 8. Zahuapan: mean annual plots of GR4H internal variables at 24-h, 324 and 24t time steps in reference and future periods. See Appendix B for the definition of the variables. Except for the rates, variables are expressed in $m^3\ s^{-1}$.

storms. Finally, during prolonged synoptic rainfall events ($D = \varnothing$), both 24-h and 324 simulations converge, producing similar daily values of P_{n_t} and E_{n_t}. Also, the seasonality of the difference between $P_{n_t}^{(24)}$ and $P_{n_t}^{(324)}$ is higher in the future, because of changes in the precipitation pattern during the first rainfall season: the reduced June-July precipitation in the future is concentrated over shorter discrete events. Indeed, the future net precipitation $P_{n_t}^{(24)}$ ($= P_{n_t}^{(24t)}$) accounts for only 51% of $P_{n_t}^{(324)}$ in June during the first rainfall season, and 78% in September during the second rainfall season.

• *Amplification of the time step impact during the future period by the hysteresis filling of the stores.* A slight hysteresis effect in the production storage level—due to the faster filling at the 3-h time step—results in 24t storage levels $S_t^{(24t)}$ slightly lower than $S_t^{(324)}$ at the beginning of the rainfall season in May, and slightly higher at the end, in October (Fig. 8(c)), when the storage nears full capacity. The difference is accentuated in May-July in the future period, when more short-duration rainfall is filtered by the 24t time step. 24t infiltration rate $P_{s_t}^{(24t)}/P_{n_t}^{(24t)}$ is therefore slightly higher than 324 $P_{s_t}^{(324)}/P_{n_t}^{(324)}$ at the beginning of the rainfall season in May, and lower at the end, in October (Fig. 8(d)). Similarly, the 24t evaporation rate ($E_{s_t}^{(24t)}/E_{n_t}^{(24t)}$) is slightly lower than the 324 ($E_{s_t}^{(324)}/E_{n_t}^{(324)}$) at the beginning of the rainfall season in May, and higher at the end of the season, in October (Fig. 8(e)). The difference is again accentuated in May-July. The final budget—net infiltration $P_{s_t}^{(24t)}$ minus effective evaporation $E_{s_t}^{24t}$—leads to a rather similar amount of the net precipitation entering the production store at both the 24t and the 324 time steps, in both the reference and future periods (Fig. 8(f)). Since the 324 net precipitation is higher, the available runoff at 324 $P_{r_t}^{(324)}$ is thereby also higher than $P_{r_t}^{(24t)}$ (Fig. 8(g)). The 24t routing storage level is consequently lower than the 324 level, particularly during the future May-July period (Fig. 8(h)).

The 24t and 324 simulations show different behaviors for the routing of the available runoff P_{r_t} as well. Receiving less runoff $P_{r_t}^{(24t)}$, the 24t routing reservoir produces less water exchange $F_t^{(24t)}$ than that of the 324 (Fig. 8(i)), finally leading to higher outflow during the second rainfall season peak ($Q_{r_t}^{(24t)} > Q_{r_t}^{(324)}$), while the outflow is lower during the first rainfall peak.

• *Impact at the event scale.* Fig. 9 shows an example at the event scale. The top and bottom rows each show a representative event from the first and second rainfall seasons, respectively. These events were selected from the historical period, in order to compare the simulations to observed flows (Fig. 9(f) and (l)). Typical June rainfall events are shorter than a day, resulting in higher 324 net precipitation $P_{n_t}^{(324)}$ compared to $P_{n_t}^{(24t)}$ (Fig. 9(a)). June, 27 to 29 even display zero for $P_{n_t}^{(24t)}$ while $P_{n_t}^{(324)}$ is nonzero. This results in both storage filling and runoff production at the 324 time step for this period (Fig. 9(c)), while both variables are zero at 24-h time step, regardless of the parameter set (Fig. 9(d) and (e)). This illustrates how 3-h and 324 production storages are filling faster than 24-h and 24t storages during short duration rainfalls. During the

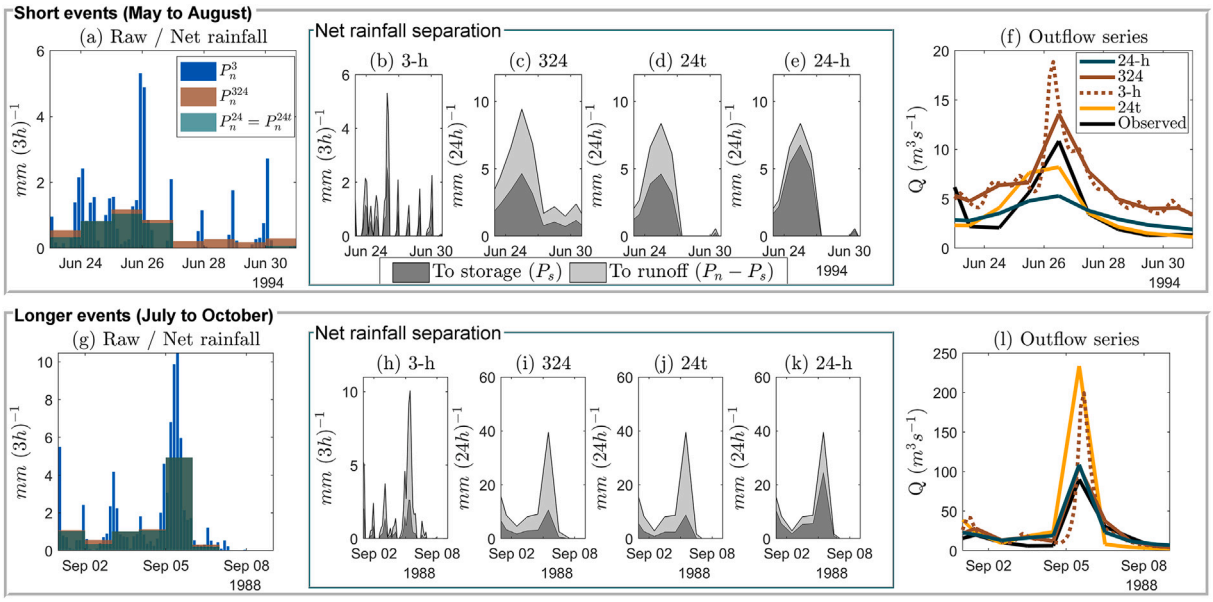

Fig. 9. Zahuapan: simulation of two historical events from the early and late rainfall seasons. (a,g): Raw and net rainfall at 3-h, 24-h and 324 time steps. (b) to (e), and (h) to (k): separation of the net rainfall with 3-h, 324, 24t and 24-h simulations. (f,l): Outflows of the four simulations compared to observed flows.

intense June, 25–26 event also, $P_{n_t}^{(24t)}$ is lower than $P_{n_t}^{(324)}$ (Fig. 9(a)), leading to both lower entry to the storage $P_{s_t}^{(24t)}$ and lower available runoff $P_{n_t}^{(24t)} - P_{s_t}^{(24t)}$ (Fig. 9(c) and (d)). The resulting 24t flood is lower than the 324 one (Fig. 9(f)). Besides, being the net precipitations $P_{n_t}^{(24)}$ and $P_{n_t}^{(24t)}$ equal, but the storage capacity $x_1^{(24)}$ higher, a larger portion of $P_{n_t}^{(24)}$ is directed to the storage compared to the 24t simulation (Fig. 9(d)). It results in a lower flood peak at 24-h than at 24t (Fig. 9(f)). Both 324 and 24t better simulate the observed flood peak than 24-h, even though they overestimate and underestimate the peak, respectively.

The second event (bottom row in Fig. 9) lasts longer than one day, resulting in nearly the same net precipitation P_{n_t} across all simulations (Fig. 9(g)). The separation between production storage and available runoff is therefore quite similar at 324 and 24t time steps (Fig. 9(i) and (j)). Despite this, the 24t outflow is more than twice as high as the 324 (Fig. 9(l)). The explanation lies in the time step dependency of the numerical solving of the sequential runoff-routing equations (Eqs. B.15–B.18). At each interval, losses from the routing store F_{n_t} —an increasing function of the routing storage level (Eq. B.15)—are computed from the previous time step storage level. The routing storage level is then modified by adding the available runoff P_{r_t} and subtracting the losses F_{n_t}. The outflow is a function of this modified routing storage level. On September 5, when the routing storage receives the available runoff P_{r_t}, the daily loss in both the 24-h and 24t simulations is calculated from the baseline 70% storage level and is therefore quite low (Fig. 10(b)) in the Supplementary Material). The store is next recharged by the incoming runoff P_{r_t}, net of those low computed losses. It reaches very high levels of 135% (24-h) and 182% (24t) of the one-day-ahead store capacities $x_3^{(24)}$ and $x_3^{(24t)}$ (Fig. 10(c)). The outflow computed from the 24t high level is then also very high (Fig. 9(l)). So are the losses computed the next day on September 6 from this same high store level, are also the 24t routing storage level falls sharply to about 63% (Fig. 10(d)). The lower exchange coefficient $x_2^{(24)}$ compared to $x_2^{(24t)}$ allows for a lower variability of the routing storage level $R_t^{(24)}$ compared to $R_t^{(24t)}$ and a lower outflow. In other words, in the 24-h and 24t simulations, the lagged losses following the main runoff event produce a large outflow on the first day of rainfall, September 5, storage depletion on September 6, and high variability in the routing store level.

For the 3-h time step, the same processes occur but are temporally shifted: peak outflow on September 5 falls in the 15–18 h interval (Fig. 10(c)), with maximum losses following in the 18–21 h interval (Fig. 10(b)). The losses increase from interval to interval as the reservoir fills up, and the total loss for the June 5–6 event is 23% higher in the 3-h simulation than in the 24t, although they share the same parameters and start at the same routing store level. Consequently, the interplay between runoff and losses shows a more gradual rise and fall, and the 3-h routing store never reaches the magnitude or variability observed in the 24t simulation. Finally, at the 324 scale, daily-averaging filters the lag between runoff and losses, causing their peaks to take place on the same day.

These examples explain the differences between the daily calibrated parameter set $x^{(24)}$ and the transferred parameter set $x^{(24t)}$: $x^{(24t)}$ underestimates low-flow conditions in the dry season and overestimates flood peaks in the storm season (Figure S.6 in the Supplementary Material). To compensate for this, daily calibration includes (1) a larger production store to attenuate the runoff entering the routing store ($x_1^{(24)}$ = 659.3mm whereas $x_1^{(24t)}$ = 152.2mm), and (2) reduced loss rates to preserve comparable routing-store levels ($x_2^{(24)}$ = −3.3mm d^{-1} whereas x_2^{24t} = −10mm d^{-1}, see Table S.3 in the Supplementary Material).

3.2.2. War eagle creek watershed: time-step dependent solving of nonlinear equations (MOHYSE)

This case study focuses on a small southern watershed simulated using MOHYSE (Fig. 11). For the convective season with low base flow (June-October), MOHYSE projects a significant increase in the return flows in the 324 simulation ($\Delta Q_{100}^{(324)}$ = +69%) , but a slight decrease in the 24-h simulation ($\Delta Q_{100}^{(24)}$ = −4%). The 324 and 24-h simulations have similar calibration performance ($KGE_c^{(24)} = KGE_c^{(324)} = 0.71$), despite differences in the calibrated values of several parameters (see Table S.4). Although the unsaturated zone capacity ($V_{\max}$) is low for both simulations, the 24-h configuration's $V_{\max}$ is roughly half of the 3-h simulation's. The time-to-peak in the 24-h simulation is approximately twice that of the 3-h simulation: $t_p^{(3)}$ = 17.1 h, (in line with the Bransby-Williams empirical concentration time) compared to $t_p^{(24)}$ = 33.8 h. The 24-h simulation's potential evapotranspiration coefficient $c_{\text{ETP}}^{(24)}$ is 1.5

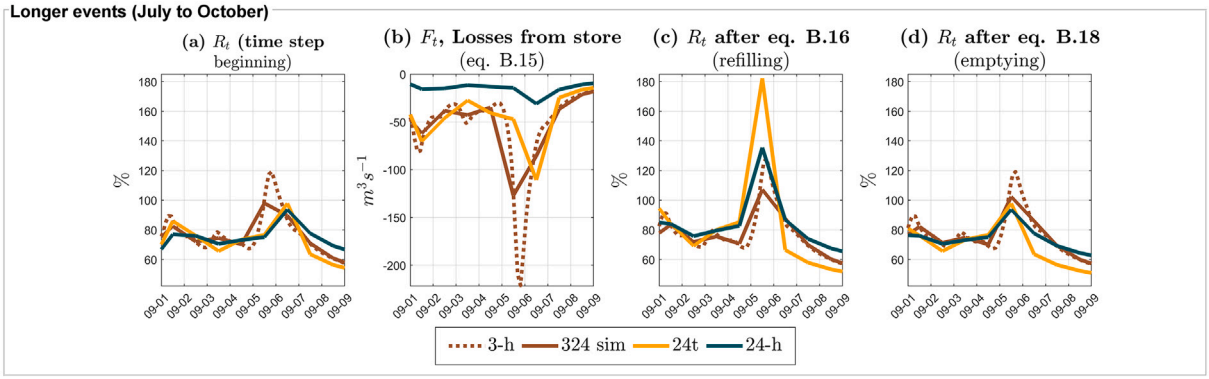

Fig. 10. Zahuapan: GR4H simulation of a rare event from the late rainfall season. Completes Fig. 9 showing the behavior of routing stores for 3-h, 324, 24t and 24-h simulations. (a): routing store level at the beginning of the time step (R_{0_t}). (b): losses F_t computed from R_0 level with Eq. (B.15). (c): routing store level R_{1_t} after refilling with the available runoff P_{r_t} and removing losses F_t to R_{0_t} (Eq. B.16). (d): routing store level R_{2_t} after routing the runoff to the outlet (Eq. B.18).

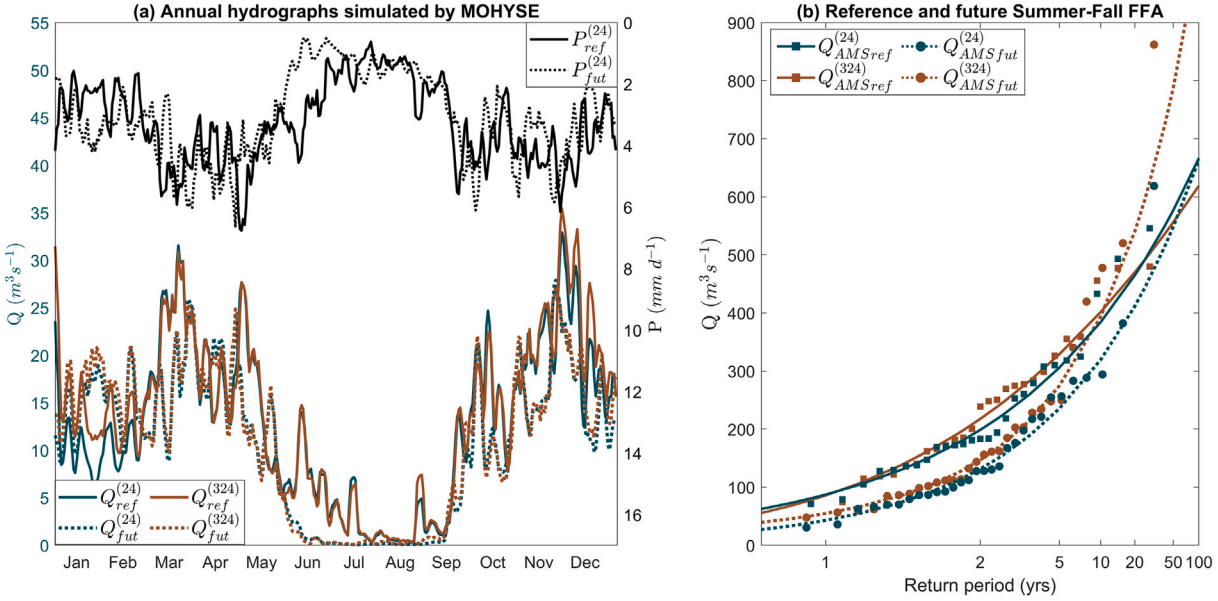

Fig. 11. Opposing climate change effects on the daily floods in War Eagle Creek, for the summer-fall season (June to October). (a): Mean annual hydrographs and hyetographs for the reference and future periods based on MOHYSE simulations at 24-h and at 324. (b): Summer-Fall FFA-AMS for simulated reference/future climates (Log Pearson III distributions). Uncertainty margins related to the return floods are not shown to improve readability.

times $c_{\mathrm{ETP}}^{(24t)}$, while the potential transpiration coefficient $c_{\mathrm{TR}}^{(24)}$ is 10 times lower than $c_{\mathrm{TR}}^{(24t)}$.

Despite these differences, the mean annual hydrographs remain similar for the 324 and 24-h simulations in the reference and future periods (Fig. 11(a)). During the convective (June-October) season, the climate simulation projects storms of increased intensity but reduced volume in the future, as evidenced by the higher maximum 3-h precipitation ($\Delta RX_3 = +14\%$) and lower maximum daily precipitation ($\Delta RX_{24} = -6\%$), as well as seasonal volumes ($\Delta\overline{P} = -16\%$). These shifts in precipitation cause a 36% decrease in mean flow for both simulations, and opposite 324 and 24-h flood projections. Although the FFA in Fig. 11(b) shows a decrease in flood magnitude across lower quantiles in both 324 and 24-h simulations, the reference rarest floods are lower at 324 than those of 24-h, yet the future rarest floods are notably higher at 324 than at 24-h. The resulting different asymmetry of the 324 and 24-h flood distributions is responsible for the opposite projections.

As in the Zahuapan watershed, these differences can be explained by the different internal processes of 3-h and 24-h simulations. The rarest flood event in the future period is presented as an example for various configurations in Fig. 12(a)–(d). Fig. 12(b) and (c) show that the 324 simulation produces a peak discharge $Q_t^{(324)}$ 39% higher than $Q_t^{(24)}$, even though the available runoff pulses $H^{(324)}$ and $H^{(24)}$ are similar. The difference in peak projections is therefore mainly attributable to the unit hydrograph routing: the 24-h simulation's longer time-to-peak ($t_p^{(24)} = 33$ h) delays and attenuates the flood pulse compared to the 324 setup ($t_p^{(3)} = 17$ h). The 24t flood peak (Fig. 12(d)) is also attenuated compared to the 324 peak, though for a different reason: higher infiltration of the raw precipitation results in less available runoff $H_t^{(24t)}$. In the 24t simulation, 29% of the raw precipitation infiltrates to the unsaturated zone, compared to 12% in the 324 configuration and 16% in the 24-h configuration.

This higher infiltration in the 24t simulation arises from the same cause as the higher 24t variability of the GR4H routing storage seen in the Zahuapan watershed: the nonlinear sequential formulation of the MOHYSE infiltration rate. Over this long event, the 3-h unsaturated zone progressively fills up, causing the net infiltration rate to decrease during

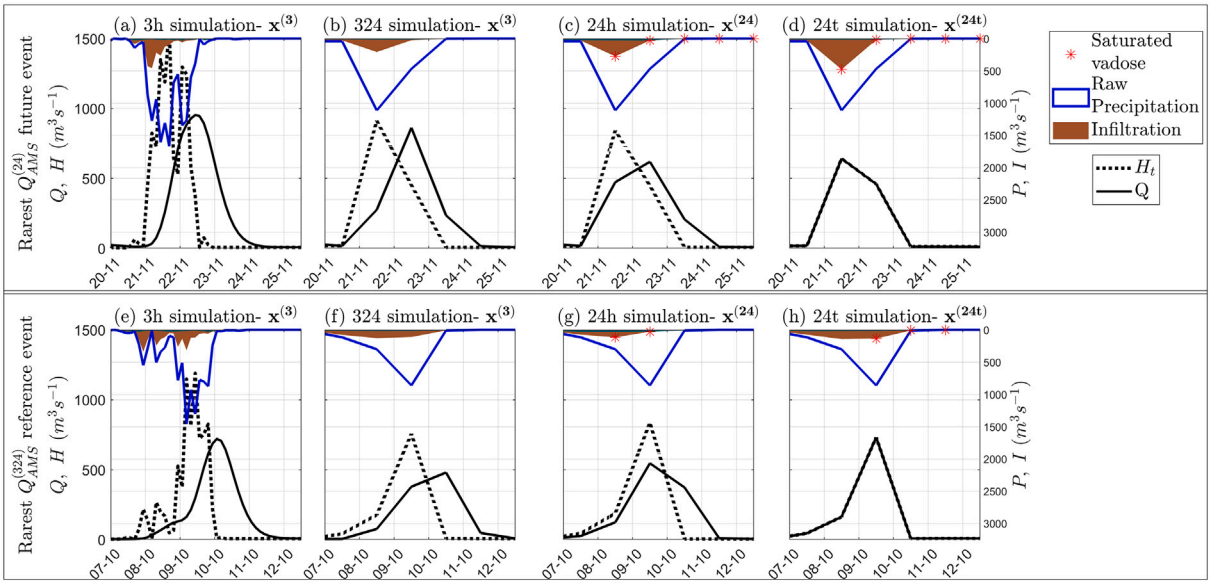

Fig. 12. War Eagle Creek: most extreme floods from the future (top row) and reference (bottom row) time series are simulated: at 3-h (a, e); at 324 (b, f); at 24-h (c, g); and at 24t (d, h). On the upper x-axis, the incoming raw precipitation is separated into infiltration, and net precipitation. There is no significant snowmelt in this watershed. H_t is the water available for runoff before transfer in the unit hydrograph (net precipitation plus contributions from the unsaturated zone and the aquifer, see Appendix A). All variables are in $m^3\ s^{-1}$ for comparison purposes.

the day. Conversely, in the daily simulations, the infiltration rate depends only on the level of the unsaturated zone at the beginning of the day, yielding a higher total daily infiltration in the 24t than in the 324 simulation. The 24-h calibration compensates for the daily higher infiltration with a lower saturated zone capacity $V^{(24)}_{max}$. The opposition with the previously shown GR4H 24-h compensatory adjustment (larger 24-h production storage) can be explained by the fact that MOHYSE uses a yes/no switch to partition precipitation to infiltration, as opposed to the hysteresis curve of GR4H. This results in higher MOHYSE unsaturated zone levels for the 24t than for the 324 simulation across the year (see Figure S.7e). Figure S.7d) also shows the thereby lower 24-h infiltration $I^{(24)}_t$ compared to $I^{(24t)}_t$ and $I^{(324)}_t$. 24-h floods are then attenuated by a longer time-to-peak of the unit hydrograph $t^{(24)}_p$ (Fig. 12(c)).

The 24-h MOHYSE calibration on the previously presented Morpions watershed notably yields the same adjustments (i.e., a reduced infiltration capacity and a longer time to peak compared to the 3-h parameters, see Table S.2 in the Supplementary Material).

Fig. 12(e)–(h) present the same type of comparisons, but this time for the rarest event in the reference period, which is also a long-duration event (54 h, 162 mm). The highest flood discharge is generated by the 24-h model rather than the 324 model (546 $m^3\ s^{-1}$ versus 480 $m^3\ s^{-1}$ for the 324), due to the specific shape of the hyetograph in this event. The hyetograph initially produces an available runoff $H^{(24)}_t$ that is 11% higher than that in the 324 simulation: on October 8 a rainfall amount of 38 mm saturates the 24-h unsaturated zone (Fig. 12(c)) but not the larger one of the 3-h simulation (Fig. 12(b) and (d)). On October 9, when the bulk of the precipitation occurs (109 mm), the rainfall is entirely directed to $H^{(24)}_t$ in the 24-h simulation, whereas it is partially infiltrated in the 324 and 24t simulations. Moreover, the shape of the hyetograph leads to a flood peak at 3-h occurring during the [0–3] UTC interval. When daily-averaging, the flood volume is spread over two days—October 9 and 10—resulting in a flattened peak in the 324 simulation compared to the 24-h configuration. October 8's rainfall drives the 24t saturated zone to 86% capacity by the end of the day, which in turn reduces infiltration on Day 2 of the event. Unlike the first event, where most precipitation fell on Day 1, available runoff H_t at 24t is nearly the same as in the 324 simulation on Day 2. As the 24t unit hydrograph does not attenuate the H_t pulses, the 24t flood peak surpasses the 324 peak.

4. Summary and discussion

We presented five case studies from diverse hydroclimatic contexts across North America, simulated by two lumped conceptual hydrological models: GR4H and MOHYSE. The objective was to demonstrate how the choice of the simulation time step can lead to opposite projections of flow metrics. We categorized the underlying causes into four distinct groups:

- The filtering of hydroclimatic processes whose characteristic times are shorter than the simulation time step, such as the diurnal cycle of the snowmelt, and short and intense convective rainfall;
- The time-step dependent solving of nonlinear equations defined by logical conditions such as *if the rain depth is higher than the potential evapotranspiration then…, otherwise* …; or: *if storage is full then …, otherwise* …). For example, both GR4H and MOHYSE showed a higher net precipitation produced from short events at the finer time step, similar to the XAJ model in Zhao et al. (2023), leading to both event-scale and long-term differences between 324 and 24-h simulations in the future;
- The time-step dependent solving of nonlinear sequential equations. The discretized water balance equations governing storage evolution led to differences between the 24-h and 324 time series. As the water depth entering a storage depends on the storage level, the total daily infiltration from a rainfall event was found to be lower at the finer 3-h temporal discretization. The consequences on the storage levels at the seasonal scale were found to differ for GR4H and MOHYSE, as GR4H's storage follows a hysteresis curve whereas MOHYSE's storage inputs are made following a binary decision. GR4H 324 storage levels presented a higher seasonal variability than that of 24t, while MOHYSE 24t storage reaches higher levels than that of 324 throughout the year. These differences between 324 and 24t levels affect runoff production at both the event-scale, and the long-term scale;
- The non-autosimilarity in flood simulation across temporal resolutions, due to the placement of the time-step window relative to the event timing. This non-autosimilarity was identified between 3-h and 324 floods: a 3-h peak occurring near midnight is heavily smoothed by the 24-h averaging, whereas the same event

peaking at twelve is better scaled by the averaging. Temporal non-autosimilarity also arises between 24-h floods simulated in different time references (LST vs. UTC), because the 24-h aggregation reshapes the precipitation time series that drives the hydrological model.

The potential consecutive divergences between future simulation time steps vary by climate regime and climate change type, and do not manifest uniformly. The causes of divergences may also combine to produce a compound effect, or to cancel out their respective effects.

4.1. External vs. internal causes of divergences

Divergences between 3-h, 324 and 24-h projections in Sections 3.1.2 and 3.1.3 arise primarily from rainfall events variability rather than hydrological model parameters. These discrepancies are associated with the temporal characteristics of precipitation time series, and can be observed in both reference and future periods. More frequent short-duration storms and amplified diurnal cycle precipitation projected in the future are likely to increase this type of divergence in many regions. Daily simulations therefore are not recommended to compute design floods in such climate conditions, as they distort the relation between rainfall event structures and the watershed response.

For their part, divergences between 324 and 24-h projections from the Sections 3.1.1, 3.2.1 and 3.2.2 arise from the distinct internal processes of the 3-h and 24-h models. Because of the time-step dependent solving of the discretized equations, internal compensatory adjustments are necessary to achieve a similar calibration performance in 3-h and 24-h simulations, resulting in distinct parameter sets. For instance, in the GR4H Zahuapan watershed case, high 24t runoff caused by the routing storage dynamics was compensated in the 24-h calibration by a larger production storage parameter (x_1) and reduced losses through neighboring watersheds (x_2) compared to the 3-h time step. In contrast, the MOHYSE War Eagle Creek watershed 24-h simulation achieved compensation by reducing the maximum infiltration storage parameter ($V_{\max}$) and lengthening the time-to-peak (t_p). For the Morpions watershed, MOHYSE 24-h calibration led to a lower snowmelt temperature (T_f parameter) and a reduced snowmelt coefficient (c_f parameter) to compensate for the filtered diurnal cycle of snowmelt.

4.2. Consequences of the compensatory mechanisms in climate change

Interdependencies between climate and watershed characteristics produce varying responses of the compensation processes to climate change signals, depending on the watershed and the hydrological model, possibly resulting in divergent behaviors of 324 and 24-h simulations in the future. In other words, the parameter sets optimized by 24-h and 3-h calibrations are set to produce similar simulations at 24 and 3-h time steps for the calibration period, meaning the distinct parameters at both time steps effectively compensate for the distinct solving of non-linear equations on outflows in this particular climate. A divergence between 24-h and 324 future simulations, whether on average or extreme values, shows that at least one simulation falls outside this domain of validity. We have presented a series of examples to illustrate this behavior, both at the event-scale and at the seasonal scale. In the War Eagle Creek watershed case, for example, the future high-volume storms rarely observed during the calibration phase resulted in the recurring saturation of the MOHYSE infiltration storage. In the Zahuapan watershed, a shift in precipitation seasonality produced distinct 324 and 24 future hydrographs. Changes in the seasonal precipitation distribution and in the statistical characteristics of rainfall events led to divergences in the long-term compensatory adjustments, causing discrepancies between future 324 and 24-h simulations. Rising temperature, and the consequent increase in potential evapotranspiration, created discrepancies between future 324 and 24-h global water budgets in watersheds where subdaily rainfall is frequent. In the entire sample from which the case studies are taken, 73% of the future changes in annual mean flow were larger in the 324 version than in the 24-h one.

4.3. Multi-resolution simulations, a method for detecting shifts in simulated hydroclimatic regimes

Comparing simulations at different time steps is not only a useful method for understanding the compensatory mechanisms that allow similar performance of the simulations at different time steps in calibration of lumped hydrological models, but also an excellent way to examine a parameter set's domain of validity. The present study highlights notably inconsistent cases between 24-h and 324 simulations (opposite projections). Simulating climate change at different time steps in a watershed, and observing a divergence despite similar simulations during the reference period, seems to be a meaningful red flag to detect projections that require an expert perspective before being used for engineering purposes. Our findings suggest the inclusion of simulations at different time steps in the methodology to calculate future hydrological metrics in a watershed, as a precautionary measure.

Furthermore, one could design an experiment in which synthetic climates systematically force 3-h, 24t and 24-h simulations to define the domain of validity for those compensatory adjustments. Successive synthetic climates with distinct statistical properties (e.g., by increasing average temperatures, or precipitation volumes at the seasonal and event scales) could be tested to determine a validity threshold based on when simulations diverge between 324 and 24-h time steps in average and in extreme hydrological metrics. Ji et al. (2023)'s review on the non-stationarity of hydrological models indicates that a lumped hydrological model should not be applied to climates differing by at least 10% in annual precipitation or 1.75 °C from the calibration climate. The proposed experiment of this research could help refine such conservative recommendations for a variety of hydroclimatic contexts.

4.4. On the importance of analyzing outlier-generating processes

This study showed that opposite projections of flood metrics ($\Delta\overline{Q_{AMS}}$ and ΔQ_{100}) computed from 24-h and 324 simulations often emerge from only one or two of the rarest floods of the time series. Indeed, the rare floods are more likely to fall outside the domain of validity of the parameter sets, and the compensatory adjustments can fail in this case. These outliers may become more frequent in the future for drier or wetter climates (impacting the initial conditions of the events) or due to the intensification of the precipitation, which is more pronounced at finer time steps (Lenderink et al., 2017; Najibi et al., 2022). Outliers can also arise from increased rainfall volumes due to clustered events, which are projected to become more frequent in the future (Du et al., 2022).

This paper identified two primary cases of divergences regarding outliers: mixed rainfall-snowmelt events, and clustered summer-fall events. In both instances, either the 324 or the 24-h simulation could produce the highest outlier, depending on the event timing, rendering projections of these kinds of events highly unstable across climate simulations. The thereby substantial difference between peak values at 324 and 24-h time steps is enough to alter statistical characteristics of the annual maxima series like mean, skewness and kurtosis, leading to discrepancies in 324 versus 24-h annual maxima and return flows. As an example, in the full sample of 221 watersheds, 39% of the indices of change in 100-year floods differ by at least 25% between 324 and 24-h computations, while 17% of these indices differ by at least 50% between 324 and 24-h computations.

4.5. Finer resolution does not necessarily equal better performance

Although a finer resolution appears more physically realistic —better capturing diurnal cycles and short-duration events—and reduces numerical discretization errors, it does not always yield the best performance in lumped conceptual hydrological models, depending on the chosen performance metrics, model, and the hydroclimatic regime (Ficchì et al., 2019; Destuynder, 2025). For MOHYSE, for example, while the 324

simulation of future snowmelt in the Morpions watershed seems more reliable than the 24-h version, it remains difficult to determine whether the 324 or 24-h future hydrograph more accurately simulates the actual response to changes in the precipitation regime in the War Eagle Creek watershed. Answering this question would require understanding the actual soil infiltration capacity and the behavior of this watershed's unsaturated zone.

The critical role of the groundwater storage capacities in driving divergences between future 324 and 24-h simulations highlights a specific concern: current automatic calibration procedures cannot accurately estimate the actual capacities in many watersheds where these capacities have not been frequently reached in the past. This leads to high uncertainty in simulated future floods. The future floods can be overestimated when the calibrated capacity is underestimated, and vice versa. The demonstrated importance of the saturation threshold also questions the reliability of lumped modeling of watersheds with spatially heterogeneous soil capacities in wetter climates. Studying the relationship between the calibrated storage capacities of diverse modeling structures at varying temporal resolutions and the thresholds that trigger Hortonian and Dunne saturation flows on an experimental watershed, following the approach of Sinha et al. (2016)'s experiments, would help assess the reliability of the models in changing climates.

4.6. Conclusion

Observing very different or even opposite climate change signals in 3-h, 324 and 24-h flow metrics underscores the need for an in-depth analysis of the watershed prior to drawing any conclusions about future flood projections. Noting these divergent simulations also offers a valuable approach for understanding the behavior of lumped hydrological models in non-stationary climatic conditions, when inflow/outflow budgets and seasonal storage patterns are affected by climate change. Both GR4H and MOHYSE simulations showed identifiable compensatory adjustments for the diurnal cycles (snowmelt, evapotranspiration-precipitation budget). Both adapted the groundwater storage capacity to compensate for the different amounts of infiltration resulting from the sequential equations at 324 and 24-h time steps. The consequent contradictory storage capacities were responsible for divergences in the future when the change in the precipitation patterns led to the storage saturation at one time step only. This raises the need to ensure a physically-based representation of the saturation threshold during the calibration in order to improve the reliability of hydrological simulations in climate change studies. This study also showed that the time step effects on the hydrological simulations are not confined to small, highly reactive watersheds: changes in the seasonality of the precipitation regime, the increasing frequency of short-duration rainfalls, or compound and mixed events, and the specific characteristics of climate change can also introduce time-step dependencies in large watersheds.

CRediT authorship contribution statement

Virginie Destuynder: Writing – review & editing, Writing – original draft, Visualization, Validation, Investigation, Conceptualization. **Siavash Pouryousefi Markhali:** Writing – review & editing. **Annie Poulin:** Writing – review & editing, Supervision.

Declaration of competing interest

The authors declare the following financial interests/personal relationships which may be considered as potential competing interests:

Virginie Destuynder reports that financial support was provided by Quebec Ministry of the Economy and Innovation. Virginie Destuynder also reports that financial support was provided by Ouranos Inc. If there are other authors, they declare that they have no known competing financial interests or personal relationships that could have appeared to influence the work reported in this paper.

Acknowledgement

This study has been partly funded by the Québec Ministère de l'Économie, de l'Innovation et de l'Énergie (MEIE) –PSR-SIIRI-955 Project, and by the Consortium Ouranos –510024 Project.

Appendix A. MOHYSE model

The internal structure of MOHYSE is summarized in Fig. A.1. The variables are presented in Table A.4 where they are categorized as input variables, internal variables (storage levels and transient flows) and output variables. The automatically calibrated parameters are defined in Table A.5, as well as the constants employed in the equations. These equations are detailed in Appendix A.1.

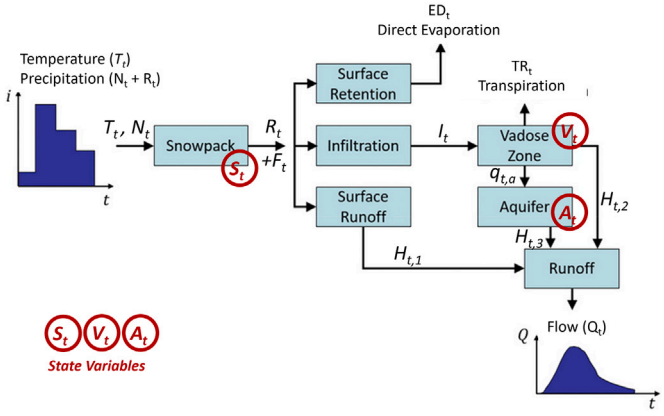

Fig. A.1. MOHYSE structure, adapted from Fortin and Turcotte (2006).

Table A.4
MOHYSE variables.

Variable	Unit	Definition
Input variables		
T_t	°C	Mean temperature of the time step t
R_t	mmΔt^{-1}	Total rain of the time step t
N_t	mmΔt^{-1}	Total snowfall of the time step t
j_t	d	Julian day of the time step t
Storage level state variables		
S_t	mm	Snow water equivalent at the end of time step t
V_t	mm	unsaturated zone level at the end of time step t
A_t	mm	Aquifer level at the end of time step t
Transient flow variables		
δ_{j_t}	°	Solar declination of the time step t
ETP_t	mmΔt^{-1}	Potential evapotranspiration of the time step t
ED_t	mmΔt^{-1}	Direct evaporation of the time step t
TR_t	mmΔt^{-1}	Transpiration from the unsaturated zone of the time step t
F_t	mmΔt^{-1}	Snowmelt of the time step t
I_t	mmΔt^{-1}	Infiltration of the time step t
$H_{t,1}$	mmΔt^{-1}	Surface runoff of the time step t
$H_{t,2}$	mmΔt^{-1}	Hypodermic runoff from unsaturated zone of the time step t
$H_{t,3}$	mmΔt^{-1}	Base runoff from aquifer zone of the time step t
H_t	mmΔt^{-1}	Total production of the time step t: $H_t = H_{t,1} + H_{t,1} + H_{t,1}$
q_t	mmΔt^{-1}	Percolation from unsaturated zone to the aquifer of the time step t
Output variable		
Q_t	m^3 s^{-1}	Output flow

Table A.5
MOHYSE constants and parameters.

Parameter	Unit	Definition	Bounds (24-h)	Bounds (3-h)
Calibrated parameters and bounding intervals				
c_{ETP}	$mm\Delta t^{-1}$	PET adjustment coefficient	[0.01, 20]	[0.01, 2.5]
c_{TR}	Δt^{-1}	Transpiration coefficient	[0.01, 1]	"
c_f	$mm°C^{-1}\Delta t^{-1}$	Snowmelt rate	[0.01, 20]	[0.01, 2.5]
T_f	°C	Snowmelt threshold	[−5, 5]	"
V_{max}	mm	Maximal height of the unsaturated zone	[0.01, 500]	"
c_{va}	Δt^{-1}	unsaturated zone to the aquifer transfer coefficient	[0.01, 1]	"
c_v	Δt^{-1}	unsaturated zone to river transfer coefficient	[0.01, 1]	"
c_a	Δt^{-1}	Aquifer to river transfer coefficient	[0.01, 1]	"
α	–	Unit hydrograph shape coefficient	[0.01, 15]	"
β	–	Unit hydrograph scale coefficient	[0.01, 15]	"
Constants				
L	°	Mean latitude of the watershed		
B	km^2	Watershed area		
K	Δt	Maximal response time of the watershed		
Δt	h	Discretization time step duration		

A.1. MOHYSE's equations

The total production is transferred to the outlet through a Nash unit hydrograph U:

$$\forall k \in 1 \dots K, U(k) = \frac{k^{\alpha-1} exp^{-k/\beta}}{\sum_{k=1}^{K} k^{\alpha-1} exp^{-k/\beta}} \tag{A.1}$$

The discretized equations are iterated for each time step t after initialization of the internal variables to zero.

$$\delta_{j_t} = 0,41 \sin\left(\frac{j_t - 80}{365} 2\pi\right) \tag{A.2}$$

$$ETP_t = \frac{c_{ETP}}{\pi} \arccos\left(-\tan\left(\frac{L\pi}{180}\right)\tan(\delta_{j_t})\right) \exp\left(\frac{17.3T_t}{238 + T_t}\right) \tag{A.3}$$

$$ED_t = \min(R_t, ETP_t) \tag{A.4}$$

$$TR_t = \min(c_{TR} V_{t-1}, ETP_t - ED_t) \tag{A.5}$$

$$F_t = \min\left(c_f \max(T_t - T_f, 0), S_{t-1}\right) \tag{A.6}$$

$$S_t = S_{t-1} + Nt - F_t \tag{A.7}$$

$$I_t = \begin{cases} 0, & \text{if } V_{t-1} \geq V_{max} \\ (R_t + F_t - ED_t)\left(1 - \frac{V_{t-1}}{V_{max}}\right), & \text{otherwise} \end{cases} \tag{A.8}$$

$$H_{t,1} = R_t + F_t - ED_t - I_t \tag{A.9}$$

$$H_{t,2} = c_V V_{t-1} \tag{A.10}$$

$$H_{t,3} = c_A A_{t-1} \tag{A.11}$$

$$q_t = c_{VA} V_{t-1} \tag{A.12}$$

$$V_t = V_{t-1} + I_t - TR_t - q_t - H_{t,2} \tag{A.13}$$

$$A_t = A_{t-1} + q_t - H_{t,3} \tag{A.14}$$

$$H_t = H_{t,1} + H_{t,2} + H_{t,3} \tag{A.15}$$

$$Q_t = \frac{B}{3,6\Delta t} \sum_{k=1}^{K} H_{t-k+1} U(k) \tag{A.16}$$

Appendix B. GR4H model

The internal structure of GR4H is summarized in Fig. B.1. The variables are presented in Table B.6 where they are categorized as input variables, internal variables (storage levels and transient flows) and output variables. The automatically calibrated parameters are defined in Table B.7, as well as the constants employed in the equations. These equations are detailed in Appendix B.1.

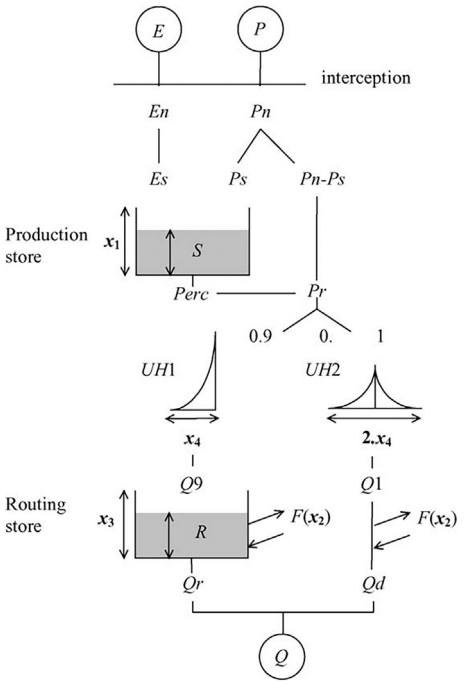

Fig. B.1. GR4H structure, Taken from (Perrin et al., 2003).

B.1. GR4H's equations

The original discretization scheme proposed at a daily time step in Perrin et al. (2003) is adapted to the time step duration Δt following Mathevet (2005). $Q_{9,t}$ and $Q_{1,t}$ are routed through two unit hydrographs $UH_{1,t}$ and $UH_{2,t}$. The hydrograph ordinates are calculated from the S curve, respectively named $SH_{1,t}$ and $SH_{2,t}$:

$$SH_{1,t} = \begin{cases} 0 & \forall\, t,\ t \leq 0 \\ \left(\frac{t}{x_4}\right)^{SH_{EXP}} & \forall\, t,\ 0 < t < x_4 \\ 1 & \forall\, t,\ t \geq x_4 \end{cases} \tag{B.1}$$

$$SH_{2,t} = \begin{cases} 0 & \forall\, t,\ t \leq 0 \\ \frac{1}{2}\left(\frac{t}{x_4}\right)^{SH_{EXP}} & \forall\, t,\ 0 < t \leq x_4 \\ 1 - \frac{1}{2}\left(2 - \frac{t}{x_4}\right)^{SH_{EXP}} & \forall\, t,\ x_4 < t < 2x_4 \\ 1 & \forall\, t,\ t \geq 2x_4 \end{cases} \tag{B.2}$$

Table B.6
GR4H variables.

Variable	Unit	Definition
Input variables		
E_t	mmΔt^{-1}	Potential evapotranspiration during t. Calculated beforehand on a daily scale (Oudin et al., 2005), and then disaggregated to Δt time step according to Parton and Logan (1981)'s hourly disaggregation scheme
P_t	mmΔt^{-1}	Equivalent water depth flowing into the watershed during t, composed of rain plus snowmelt. The daily snowmelt is calculated beforehand with the $CEMANEIGE$ algorithm (Valéry, 2010), assuming homogeneous snowmelt parameters for all altitude levels. The daily snowmelt is then disaggregated according to Parton and Logan (1981)'s hourly scheme
Storage level state variables		
S^t	mm	Production store level at the end of t
R^t	mm	Routing store level at the end of t
Transient flow variables		
P_{n_t}	mmΔt^{-1}	Net precipitation during t
E_{n_t}	mmΔt^{-1}	Net evapotranspiration capacity during t
P_{s_t}	mmΔt^{-1}	Part of the net precipitation transferred to the production storage during t
E_{s_t}	mmΔt^{-1}	Evaporation from the production storage during t
$Perc_t$	mmΔt^{-1}	Percolation leakage during t
P_{r_t}	mmΔt^{-1}	Runoff transferred to unit hydrographs during t
$Q_{9,t}$	mmΔt^{-1}	Runoff transferred to UH1 during t
$Q_{1,t}$	mmΔt^{-1}	l Runoff transferred to UH2 during t
F_t	mmΔt^{-1}	Groundwater exchange during t
Q_{r_t}	mmΔt^{-1}	Outflow resulting from UH1 after passing through the routing reservoir during t
Q_{d_t}	mmΔt^{-1}	Outflow resulting from UH2 after water exchanges during t
Output variables		
Q_{sim_t}	m^3 s^{-1}	Outflow of time step t

Table B.7
GR4H constants and parameters.

Parameter	Unit	Definition	Bounds (24-h)	Bounds (3-h)
Calibrated parameters and bounding intervals				
x_1	mm	Maximum capacity of the production store	[1, 750]	"
x_2	mmΔt^{-1}	Groundwater exchange coefficient	[−10, 10]	"
x_3	mm	One time step ahead maximum capacity of the routing store	[1, 400]	"
x_4	Δt	Time base of unit hydrograph UH1	[0.5, 10]	[0.5, 120]
x_5[a]	mm °C^{-1}	Degree-day factor	[0, 10]	"
x_6[a]	–	Thermal state coefficient	[0, 1]	"
Constants				
SH_{exp}		Time-dependent exponent in unit hydrographs UH1 and UH2. Adapted from Mathevet (2005) $SH_{exp}^{(3)} = 1.36$; $SH_{exp}^{(24)} = 2.5$.		
B	km^2	Watershed area		
Δt	h	Time step duration		

[a] x_5 and x_6 are the $CEMANEIGE$ parameters.

$$UH_{1,t} = SH_{1,t} - SH_{1,t-1} \qquad \forall\, t,\ t \in [1 \cdots x_4] \tag{B.3}$$

$$UH_{2,t} = SH_{2,t} - SH_{2,t-1} \qquad \forall\, t,\ t \in [1 \cdots 2x_4] \tag{B.4}$$

The discretized equations are solved iteratively for each time step t after initialization of the internal variables to zero:

$$P_{n_t} = \max(0, P_t - E_t) \tag{B.5}$$

$$E_{n_t} = \max(0, E_t - P_t) \tag{B.6}$$

$$P_{s_t} = \begin{cases} \dfrac{x_1\left(1-\left(\frac{S_{t-1}}{x_1}\right)^2\right)tanh\left(\frac{P_{n_t}}{x_1}\right)}{1+\frac{S_{t-1}}{x_1}tanh\left(\frac{P_{n_t}}{x_1}\right)} & \text{if } P_{n_t} > 0 \\ 0 & \text{otherwise} \end{cases} \tag{B.7}$$

$$E_{s_t} = \begin{cases} 0 & \text{if } P_{n_t} > 0 \\ \dfrac{S_{t-1}\left(2-\frac{S_{t-1}}{x_1}\right)tanh\left(\frac{E_{n_t}}{x_1}\right)}{1+\left(1-\frac{S_{t-1}}{x_1}\right)tanh\left(\frac{E_{n_t}}{x1}\right)} & \text{otherwise} \end{cases} \tag{B.8}$$

$$S_t = S_{t-1} - E_{s_t} + P_{s_t} \tag{B.9}$$

$$Perc_t = S_t\left[1 - \left(1 + \frac{\Delta t}{24}\left(\frac{9}{4}\frac{S_t}{x_1}\right)^4\right)^{-1/4}\right] \tag{B.10}$$

$$S_t = S_t - Perc_t \tag{B.11}$$

$$P_{r_t} = Perc_t + P_{n_t} - P_{s_t} \tag{B.12}$$

$$Q_{9,t} = 0,9\sum_{k=1}^{\lceil x_4 \rceil} UH_{1,k}P_{r_{t-k+1}} \tag{B.13}$$

$$Q_{1,t} = 0,1\sum_{k=1}^{\lceil 2x_4 \rceil} UH_{2,k}P_{r_{t-k+1}} \tag{B.14}$$

$$F_t = \frac{\Delta t}{24}x_2\left(\frac{R_{t-1}}{x_3}\right)^{7/2} \tag{B.15}$$

$$R_t = \max(0; R_{t-1} + Q_{9,t} + F_t) \tag{B.16}$$

$$Q_{r_t} = R_t\left(1 - \left(1 + \frac{\Delta}{24}\left(\frac{R_t}{x_3}\right)^4\right)^{-1/4}\right) \tag{B.17}$$

$$R_t = R_t - Q_{r_t} \tag{B.18}$$

$$Q_{d_t} = \max(0; Q_{1,t} + F_t) \tag{B.19}$$

$$Q_{sim_t} = \frac{B}{3,6\Delta t}(Q_{r_t} + Q_{d_t}) \tag{B.20}$$

Appendix C. Scaling of the 3-h parameters to the 24t time step

The impact of the time step on the future simulations is studied by comparing simulations run with the 3-h and 24-h calibrated parameter sets, $x^{(3)}$ and $x^{(24)}$, but also by comparing simulations run with the 3-h calibrated parameter set $x^{(3)}$ to simulations run with an equivalent parameter set transferred to the daily scale, $x^{(24t)}$. The transferred 24t parameters are obtained as follows:

Let $x_i^{(3)}$ and $x_i^{(24)}$ be the i^{th} parameters calibrated at 3-h and 24-h time steps;

Let $x_i^{(24t)}$ be the i^{th} parameter calibrated at 3-h and transferred to the 24-h time step.

GR4H

In GR4H, the internal structure is adapted to ensure consistency of the parameters between time steps, including those in the CEMANEIGE routine. $x^{(3)}$ can therefore be directly employed to force GR4H at a daily time step, simply by accounting for the need to convert the time base $x_4^{(3)}$ to the daily unit (Eq. C.2):

$$\forall i \in \{1,2,3,5,6\} \qquad x_i^{(24t)} = x_i^{(3)} \tag{C.1}$$

$$i = 4 \qquad x_i^{(24t)} = \frac{24}{3}x_i^{(3)} \tag{C.2}$$

MOHYSE

In this section, we use the notation $x_i|i = 1 \ldots 10$ to refer to the ten MOHYSE parameters described in Table A.4 ($C_{ETP}, C_{TR}, c_f, T_f, V_{max}, c_{va}, c_v, C_a, \alpha, \beta$). This is done to simplify the formulation of the Eqs. (C.3) to (C.6).

In MOHYSE, the internal structure is identical for both time steps, so parameters representing flows per time unit need to be scaled before being used at the daily time step (Eq. C.3). The consistency between the 3-h and the 24t Nash unit hydrographs was achieved by choosing Nash parameters that allow identical time-to-peaks (Eq. C.6). To this end, the 3-h calibrated shape coefficient α was retained (Eq. (C.4), $i = 9$), and the scale coefficient β ($i = 10$) was computed using the expression for the time-to-peak of a Nash hydrograph as a function of α and β (Eq. C.5). Note that, unlike GR4H's internal adjustment, this does not ensure equal daily volumes transferred by both the daily-averaged 3-h unit hydrograph and the 24t unit hydrograph. An alternative procedure could be used to define the $x^{(24t)}$ parameters to ensure such consistency. However, this does not affect the main results of the study. Finally, the 3-h calibrated snowmelt threshold and maximal height of the unsaturated zone were retained in the 24t simulation (Eq. (C.4), $i = 4, 5$).

$$\forall\, i \in \{1,2,3,6,7,8\} \qquad x_i^{(24t)} = \frac{24}{3} x_i^{(3)} \tag{C.3}$$

$$\forall\, i \in \{4,5,9\} \qquad x_i^{(24t)} = x_i^{(3)} \tag{C.4}$$

$$\forall\, i \in \{10\} \qquad x_i^{(24t)} = x_i^{(3)} \Big/ \left(\frac{24}{3} (x_9^{(3)} - 1) \right) \tag{C.5}$$

$$t_p^{(24t)} = \frac{3}{24} t_p^{(3)} \tag{C.6}$$

Appendix D. Supplementary data

Supplementary data for this article can be found online at doi:10.1016/j.jhydrol.2026.135081.

Data availability

Data will be made available on request.

References

Anderson, T.W., Darling, D.A., 1954. A test of goodness of fit. J. Am. Stat. Assoc. 49, 765–769. https://doi.org/10.1080/01621459.1954.10501232. https://www.tandfonline.com/doi/abs/10.1080/01621459.1954.10501232

Asadzadeh, M., Leon, L., Yang, W., Bosch, D., 2016. One-day offset in daily hydrologic modeling: An exploration of the issue in automatic model calibration. J. Hydrol. 534, 164–177. https://doi.org/10.1016/j.jhydrol.2015.12.056. https://www.scopus.com/inward/record.uri?eid=2-s2.0-84954482806&doi=10.1016

Astagneau, P.C., Bourgin, F., Andréassian, V., Perrin, C., 2021. When does a parsimonious model fail to simulate floods? learning from the seasonality of model bias. Hydrol. Sci. J. 66, 1288–1305. https://doi.org/10.1080/02626667.2021.1923720. https://www.scopus.com/inward/record.uri?eid=2-s2.0-85108858620&doi=10.1080

Bastola, S., Misra, V., 2013. Sensitivity of hydrological simulations of southeastern united states watersheds to temporal aggregation of rainfall. J. Hydrometeorol. 14, 1334–1344. https://doi.org/10.1175/JHM-D-12-096.1. https://www.scopus.com/inward/record.uri?eid=2-s2.0-84883813585&doi=10.1175

Beck, H.E., Wood, E.F., Pan, M., Fisher, C.K., Miralles, D.G., van Dijk, A.I.J.M., McVicar, T.R., Adler, R.F., 2019. Mswep v2 global 3-hourly 0.1° precipitation: Methodology and quantitative assessment. Bull. Am. Meteorol. Soc. 100, 473–500. https://doi.org/10.1175/bams-d-17-0138.1. https://journals.ametsoc.org/view/journals/bams/100/3/bams-d-17-0138.1.xml

Beylich, M., Haberlandt, U., Reinstorf, F., 2021. Daily vs. hourly simulation for estimating future flood peaks in mesoscale catchments. Hydrol. Res. 52, 821–833. https://doi.org/10.2166/nh.2021.152. https://www.scopus.com/inward/record.uri?eid=2-s2.0-85113528759&doi=10.2166

Bouaziz, L.J.E., Fenicia, F., Thirel, G., De Boer-Euser, T., Buitink, J., Brauer, C.C., De Niel, J., Dewals, B.J., Drogue, G., Grelier, B., Melsen, L.A., Moustakas, S., Nossent, J., Pereira, F., Sprokkereef, E., Stam, J., Weerts, A.H., Willems, P., Savenije, H.H.G., Hrachowitz, M., 2021. Behind the scenes of streamflow model performance. Hydrol. Earth Syst. Sci. 25, 1069–1095. https://doi.org/10.5194/hess-25-1069-2021. https://www.scopus.com/inward/record.uri?eid=2-s2.0-85102050884&doi=10.5194

Bransby Williams, G., 1922. Flood discharges and the dimensions of spillways in India. Eng. (Lond.) 134, 321–322.

Brighenti, T.M., Bonumá, N.B., Srinivasan, R., Chaffe, P.L.B., 2019. Simulating subdaily hydrological process with swat: a review. Hydrol. Sci. J. 64, 1415–1423. https://doi.org/10.1080/02626667.2019.1642477. https://www.scopus.com/inward/record.uri?eid=2-s2.0-85070918284&doi=10.1080

Bukovsky, M.S., 2012. Masks for the bukovsky regionalization of north america, regional integrated sciences collective. Institute for Mathematics Applied to Geosciences, National Center for Atmospheric Research, Boulder, CO. Downloaded 06–18.

Cannon, A.J., 2018. Multivariate quantile mapping bias correction: an n-dimensional probability density function transform for climate model simulations of multiple variables. Clim. Dyn. 50, 31–49. https://doi.org/10.1007/s00382-017-3580-6

Clark, M.P., Kavetski, D., 2010. Ancient numerical daemons of conceptual hydrological modeling: 1. fidelity and efficiency of time stepping schemes. Water Resour. Res. 46, https://doi.org/10.1029/2009WR008894

Comisión Federal de Electricidad, 2017. Red automática de estaciones hidroclimatológicas de la cfe. https://www.gob.mx/ineel/prensa/red-automatica-de-estaciones-hidroclimatologicas-de-la-cfe

Comisión Nacional del Agua, 2016. Banco nacional de datos de aguas superficiales (bandas). https://app.conagua.gob.mx/bandas/

De Boer-Euser, T., Bouaziz, L., De Niel, J., Brauer, C., Dewals, B., Drogue, G., Fenicia, F., Grelier, B., Nossent, J., Pereira, F., Savenije, H., Thirel, G., Willems, P., 2017. Looking beyond general metrics for model comparison - lessons from an international model intercomparison study. Hydrol. Earth Syst. Sci. 21, 423–440. https://doi.org/10.5194/hess-21-423-2017. https://www.scopus.com/inward/record.uri?eid=2-s2.0-85011008984&doi=10.5194

Destuynder, V., 2025. Facteurs de divergences entre projections hydrologiques journalières et sous-journalières de modèles hydrologiques globaux conceptuels. Thesis. École de Technologie Supérieure, Montréal.

Du, H., Donat, M.G., Zong, S., Alexander, L.V., Manzanas, R., Kruger, A., Choi, G., Salinger, J., He, H.S., Li, M.H., Fujibe, F., Nandintsetseg, B., Rehman, S., Abbas, F., Rusticucci, M., Srivastava, A., Zhai, P., Lippmann, T., Yabi, I., Stambaugh, M.C., Wang, S., Batbold, A., de Oliveira, P.T., Adrees, M., Hou, W., Santos e Silva, C.M., Lucio, P.S., Wu, Z., 2022. Extreme precipitation on consecutive days occurs more often in a warming climate. Bull. Am. Meteorol. Soc. 103, E1130–E1145. https://doi.org/10.1175/BAMS-D-21-0140.1. https://www.scopus.com/inward/record.uri?eid=2-s2.0-85129105106&doi=10.1175

Duan, Q., Sorooshian, S., Gupta, V.K., 1994. Optimal use of the sce-ua global optimization method for calibrating watershed models. J. Hydrol. 158, 265–284. https://doi.org/10.1016/0022-1694(94)90057-4

England Jr, J.F., Cohn, T.A., Faber, B.A., Stedinger, J.R., Thomas Jr, W.O., Veilleux, A.G., Kiang, J.E., Mason, J.R.R., 2019. Guidelines for determining flood flow frequency—Bulletin 17C. Report 4-B5. U. S. Geological Survey, https://doi.org/10.3133/tm4B5. http://pubs.er.usgs.gov/publication/tm4B5

Fenicia, F., Savenije, H.H.G., Matgen, P., Pfister, L., 2008. Understanding catchment behavior through stepwise model concept improvement. Water Resour. Res. 44, https://doi.org/10.1029/2006WR005563. https://agupubs.onlinelibrary.wiley.com/doi/abs/10.1029/2006WR005563

Ficchì, A., Perrin, C., Andréassian, V., 2016. Impact of temporal resolution of inputs on hydrological model performance: An analysis based on 2400 flood events. J. Hydrol. 538, 454–470. https://doi.org/10.1016/j.jhydrol.2016.04.016. https://www.sciencedirect.com/science/article/pii/S0022169416301974

Ficchì, A., Perrin, C., Andréassian, V., 2019. Hydrological modelling at multiple sub-daily time steps: Model improvement via flux-matching. J. Hydrol. 575, 1308–1327. https://doi.org/10.1016/j.jhydrol.2019.05.084. https://www.sciencedirect.com/science/article/pii/S0022169419305281

Fortin, V., Turcotte, R., 2006. Le modèle hydrologique mohyse. Note de cours pour SCA7420, Département Des Sciences de La Terre Et de L'Atmosphère, Université Du Québec à Montréal 23.

Gupta, H.V., Kling, H., Yilmaz, K.K., Martinez, G.F., 2009. Decomposition of the mean squared error and nse performance criteria: Implications for improving hydrological modelling. J. Hydrol. 377, 80–91. https://doi.org/10.1016/j.jhydrol.2009.08.003. https://www.scopus.com/inward/record.uri?eid=2-s2.0-70349272865&doi=10.1016

Hennermann, K., Berrisford, P., 2018. Era5 data documentation. https://confluence.ecmwf.int/display/CKB/ERA5

Huang, Y., Bárdossy, A., Zhang, K., 2019. Sensitivity of hydrological models to temporal and spatial resolutions of rainfall data. Hydrol. Earth Syst. Sci. 23, 2647–2663. https://doi.org/10.5194/hess-23-2647-2019. https://www.scopus.com/inward/record.uri?eid=2-s2.0-85067598183&doi=10.5194

Ji, H.K., Mirzaei, M., Lai, S.H., Dehghani, A., Dehghani, A., 2023. The robustness of conceptual rainfall-runoff modelling under climate variability – a review. J. Hydrol. 621, 129666. https://doi.org/10.1016/j.jhydrol.2023.129666. https://www.sciencedirect.com/science/article/pii/S002216942300608X

Kavetski, D., Fenicia, F., Clark, M.P., 2011. Impact of temporal data resolution on parameter inference and model identification in conceptual hydrological modeling: Insights from an experimental catchment. Water Resour. Res. 47, https://doi.org/10.1029/2010WR009525. https://www.scopus.com/inward/record.uri?eid=2-s2.0-79955964338&doi=10.1029

La Follette, P.T., Teuling, A.J., Addor, N., Clark, M., Jansen, K., Melsen, L.A., 2021. Numerical daemons of hydrological models are summoned by extreme precipitation. Hydrol. Earth Syst. Sci. 25, 5425–5446. https://doi.org/10.5194/hess-25-5425-2021. https://www.scopus.com/inward/record.uri?eid=2-s2.0-85117137479&doi=10.5194

Le Moine, N., 2008. Le bassin versant de surface vu par le souterrain: une voie d'amélioration des performances et du réalisme des modèles pluie-débit? Thesis. Doctorat Géosciences Et Ressources Naturelles, Université Pierre Et Marie.

Lenderink, G., Barbero, R., Loriaux, J.M., Fowler, H.J., 2017. Super-clausius-clapeyron scaling of extreme hourly convective precipitation and its relation to large-scale atmospheric conditions. J. Clim. 30, 6037–6052. https://doi.org/10.1175/JCLI-D-16-0808.1. https://www.scopus.com/inward/record.uri?eid=2-s2.0-85022331052&doi=10.1175

Li, X., Huang, S., He, R., Wang, G., Tan, M.L., Yang, X., Zheng, Z., 2020. Impact of temporal rainfall resolution on daily streamflow simulations in a large-sized river basin. Hydrol. Sci. J. 65, 2630–2645. https://doi.org/10.1080/02626667.2020.1836374. https://www.scopus.com/inward/record.uri?eid=2-s2.0-85095796529&doi=10.1080

Lu, Y., Tu, J., Gao, Z.G., Li, X.G., Yang, S., Yang, X.Y., 2020. Impact of temporal rainfall resolution on swat hydrological simulation. Zhongguo Huanjing Kexue/China

Environ. Sci. 40, 5383–5390. https://www.scopus.com/inward/record.uri?eid=2-s2.0-85099334776&partnerID=40&md5=51bfeb3d0647569fc5b4bdef9d62f0ad

Markhali, S.P., Poulin, A., Boucher, M.-A., 2022a. Spatio-temporal discretization uncertainty of distributed hydrological models. Hydrol. Process. 36, https://doi.org/10.1002/hyp.14635

Markhali, S.P., Poulin, A., Boucher, M.-A., Mai, J., Seibert, J., Zaerpour, M., 2022b. Multi-scale flood simulations under climate change scenarios. Authorea Preprints. [Manuscript submitted for publication].

Martel, J.L., Fortin, V., Turcotte, R., Poulin, A., Arsenault, R., 2025. Mohyse – a simple lumped hydrological model for educational and research purposes. Can. Water Resour. J. https://doi.org/10.1080/07011784.2025.2536023. https://www.scopus.com/inward/record.uri?eid=2-s2.0-105012448496&doi=10.1080

Mathevet, T., 2005. Quels modèles pluie-débit globaux au pas de temps horaire? Développements empiriques et comparaison de modèles sur un large échantillon de bassins versants. Thesis.

Ministère de l'Environnement and de la Lutte contre les changements climatiques and de la Faune et des Parcs, 2020. Stations hydrométriques de l'atlas hydroclimatique. https://www.cehq.gouv.qc.ca/atlas-hydroclimatique/stations-hydrometriques/index.htm

Najibi, N., Mukhopadhyay, S., Steinschneider, S., 2022. Precipitation scaling with temperature in the northeast us: variations by weather regime, season, and precipitation intensity. Geophys. Res. Lett. 49, https://doi.org/10.1029/2021GL097100. https://www.scopus.com/inward/record.uri?eid=2-s2.0-85129012511&doi=10.1029

Oudin, L., Hervieu, F., Michel, C., Perrin, C., Andréassian, V., Anctil, F., Loumagne, C., 2005. Which potential evapotranspiration input for a lumped rainfall–runoff model?: Part 2—towards a simple and efficient potential evapotranspiration model for rainfall–runoff modelling. J. Hydrol. 303, 290–306.

Pan, S., Xuan, W., Xu, Y.P., Gu, H., Bai, Z., 2021. Temporary dependency of parameter sensitivity for different flood types. Hydrol. Res. 52, 990–1014. https://doi.org/10.2166/nh.2021.187. https://www.scopus.com/inward/record.uri?eid=2-s2.0-85119150708&doi=10.2166

Parton, W.J., Logan, J.A., 1981. A model for diurnal variation in soil and air temperature. Agric. Meteorol. 23, 205–216.

Perrin, C., Michel, C., Andréassian, V., 2003. Improvement of a parsimonious model for streamflow simulation. J. Hydrol. 279, 275–289. https://doi.org/10.1016/s0022-1694(03)00225-7. https://www.scopus.com/inward/record.uri?eid=2-s2.0-0141682120&doi=10.1016

Sinha, S., Rode, M., Borchardt, D., 2016. Examining runoff generation processes in the selke catchment in central germany: Insights from data and semi-distributed numerical model. J. Hydrol.: Reg. Stud. 7, 38–54. https://doi.org/10.1016/j.ejrh.2016.06.002. https://www.scopus.com/inward/record.uri?eid=2-s2.0-84977490563&doi=10.1016

U.S. Geological Survey, 2021. National water information system (nwis). https://nwis.waterservices.usgs.gov/

Valéry, A., 2010. Modélisation précipitations débit sous influence nivale: Elaboration d'un module neige et évaluation sur 380 bassins versants. Thesis. Doctorat Hydrobiologie, Institut Des Sciences Et Industries Du Vivant Et de L'Environnement AgroParisTech. https://hal.inrae.fr/tel-02594605

Wang, H., Li, X., Hao, S., 2015. Effects of rainfall data resolution on watershed-scale model performance in predicting runoff. J. Water Clim. Change 6, 227–240. https://doi.org/10.2166/wcc.2014.153. https://www.scopus.com/inward/record.uri?eid=2-s2.0-84930699314&doi=10.2166

Zhao, J., Duan, Y., Hu, Y., Li, B., Liang, Z., 2023. The numerical error of the xinanjiang model. J. Hydrol. 619, 129324. https://doi.org/10.1016/j.jhydrol.2023.129324. https://www.sciencedirect.com/science/article/pii/S0022169423002664